Plant-Level Modeling and Simulation of Used Nuclear Fuel Dissolution*

Valmor F. de Almeida

Oak Ridge National Laboratory
Oak Ridge, TN 37831-6181, USA

Report ORNL/TM-2012/375

07 September 2012

*Also available by request to `dealmeidav@ornl.gov`.

Abstract

Plant-level modeling and simulation of a used nuclear fuel prototype dissolver is presented. Emphasis is given in developing a modeling and simulation approach to be explored by other processes involved in the recycle of used fuel. The commonality concepts presented in a previous communication were used to create a model and realize its software module. An initial model was established based on a theory of chemical thermomechanical network transport outlined previously. A software module prototype was developed with the required external behavior and internal mathematical structure.

Results obtained demonstrate the generality of the design approach and establish an extensible mathematical model with its corresponding software module for a wide range of dissolvers. Scale up numerical tests were made varying the type of used fuel (breeder and light-water reactors) and the capacity of dissolution ($0.5\,\mathrm{t\,d^{-1}}$ to $1.7\,\mathrm{t\,d^{-1}}$). These tests were motivated by user requirements in the area of nuclear materials safeguards. A computer module written in high-level programing languages (MATLAB and Octave) was developed, tested, and provided as open-source code (MATLAB) for integration into the Separations and Safeguards Performance Model application in development at Sandia National Laboratories.

The modeling approach presented here is intended to serve as a template for a rational modeling of all plant-level modules. This will facilitate the practical application of the commonality features underlying the unifying network transport theory proposed recently. In addition, by example, this model describes, explicitly, the needed data from sub-scale models, and logical extensions for future model development. For example, from thermodynamics, an off-line simulation of molecular dynamics could quantify partial molar volumes for the species in the liquid phase; this simulation is currently at reach for high-performance computing. From fluid mechanics, a hold-up capacity function is needed for the dissolver device; this simulation is currently at reach for computational fluid mechanics given the existing CAD geometry. From chemical transport phenomena, a simulation of the particle-scale dissolution front is needed to derive an improved solid dissolution kinetics law by predicting the local surface area change; an example was provided in this report. In addition, the associated reaction mechanisms for dissolution are presently largely untested and simplified, hence even a parallel experimental program in reaction kinetics is needed to support modeling and simulation efforts. Last but not least, a simple account of finite rates of solid feed and transfer can be readily introduced via a coupled delayed model.

These are some of the theoretical benefits of a rational plant-level modeling approach which guides the development of smaller length and time scale modeling. Practical, and other theoretical benefits have been presented on a previous report.

Contents

List of Figures

List of Tables

0 Introduction

This modeling effort tests the modeling and simulation concepts advanced recently (de Almeida, 2011) by considering a plant-level, physicochemical model of a dissolver system for used fuel dissolution. This particular fuel recycling operation presents numerous modeling challenges when incorporating subscale phenomena (Nicholson Jr., 1977; Uriarte and Rainey, 1965); therefore, the intent here is to experiment with modeling concepts while generating information for future extensions. Published modeling work in the nuclear dissolution area at the plant-level scale is scarce, the present development used elements of past research (Johnson, 1962; Lewis, 1984; Lewis and Weber, 1980), when possible, to prototype a module with an extensible structure and capability.

The presentation is systematic, following the elements for guiding the the development of a recycling plant-level module suggested by de Almeida (2011).

Another objective of the present work is to provide a model and module for the Separations and Safeguards Performance Model code (Cipiti and McDaniel, 2011; Cipiti et al., 2009) with improved predictive capability. Progress in this integration effort is described in section 6.3.

1 Plant-level localization

A recycling plant is a hierarchical assembly of systems. A dissolver device is part of the dissolution sub-system in the head-end system of a recycling plant. The dissolution sub-system is also composed of many sub-systems which are here called stations. The following major stations form the dissolution sub-system (fig. 1.1):

- dissolver/digester,
- receiver surge tank,
- hull washing,
- clarifier,
- undissolved solids (UDS) handling, and
- dissolution off-gas (DOG).

Each station entails many equipment components which makes the dissolution sub-system a major part of a recycling plant. This report focuses on a dissolver model for the core of the dissolver/digester station.

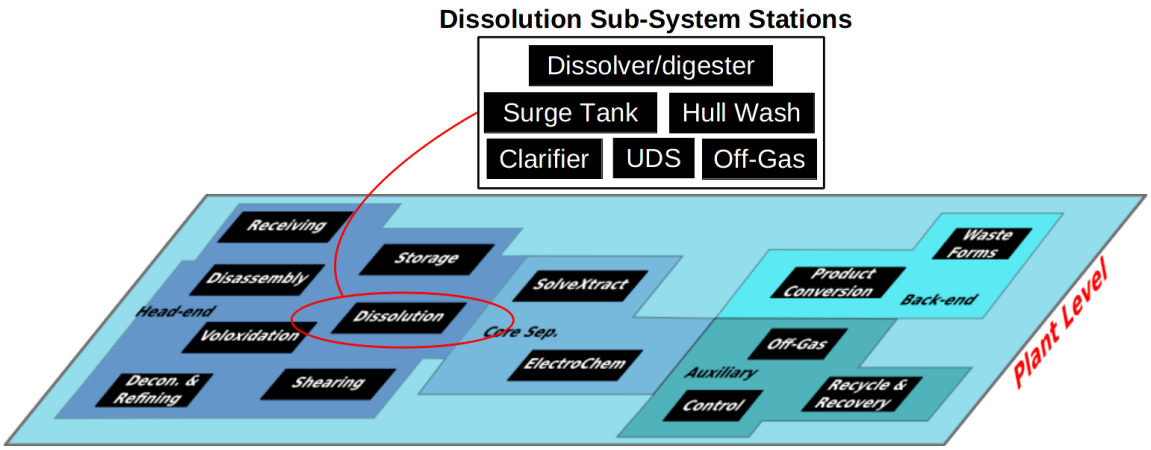

Fig. 1.1: *Localization of the dissolver/digester station in the dissolution sub-system as part of the head-end system of a recycle plant-level scale. The dissolution sub-system is organized internally as a set of six stations.*

For completeness and reference for future developments, a brief list of key equipment in each station is given here based on the ORNL Integrated Equipment Test (IET) facility (Ehinger, 1989; Yarbro et al., 1986). The dissolver/digester station houses the dissolver, digester, (fluidic) pumps, valves and spargers. The surge tank station contains a sequence of tanks connected in series, spargers, pumps, and valves. The hull washing station consists of a mechanical washer, tanks, and pumps. The clarifier station includes a solid/liquid separator for the insoluble particles, a clarified solution tank, pump (or air-lift), and valves. The UDS handling station, uses a slurry receiver tank, a sludge separator, a sludge storage tank, and (fluidic) pumps. The DOG station employs a NO_x absorber, an iodine remover, filters, pumps, a recovered acid storage tank, and auxiliary equipment. Therefore the modeling and simulation of the dissolution sub-system will require the proper consideration of relevant components in these stations and their corresponding physicochemical processes.

2 Physicochemical phenomena

This report focuses on the major component of the dissolver/digester station. The dissolver equipment is used to dissolve the bulk of the fuel rods which have been sheared into pieces by an upstream mechanical process. If a voloxidation pretreatment has been used, then the empty hulls and the fuel powder are fed to the dissolver either combined or in separated cycles. Since the dissolution process will leave the

cladding and other internal metal hardware nearly intact, the process is actually a leaching operation. The used nuclear fuel is dissolved into boiling nitric acid, HNO_3, which reacts at the surface of the solid fuel, removing metal atoms in the form of cations. There is significant complexity in this process, which involves the tumbling of pieces of sheared fuel with cladding and other fuel bundle internals in the dissolving liquid. A countercurrent, rotary contactor is one type of equipment used for industrial operations. Many prototypes have been investigated in the past (Odom, 1972). However, there is no standard contactor equipment at the time of this writing. DOE reports have been reviewed in this subject (Groenier, 1971).

A typical contactor will flow the liquid by gravity and will propel the solid pieces of sheared used fuel, or its powder (when voloxidation pretreatment is used), countercurrently. The liquid outflow contains the liquid product, and the solid outflow contains the hulls and other fuel bundle internals. The boiling temperature may be maintained by steam which participates in the recycling of nitric acid within the contactor equipment. Whether a vapor stream is used or not, the flow in the contactor involves three-phases with vapor entrainment in the liquid/solid mixture.

The dissolution of the fuel depends greatly on the type and burnup rate of the used fuel which affects the initial microstructure. Cracks in the fuel matrix (greater than $\approx 10\,\mu m$) provide highways for fluid penetration in the fuel matrix. Pretreatment of the fuel such as voloxidation will have a major effect on the efficiency of the dissolution process. It is also important to assess the release of volatile fission products into the vapor phase of the dissolver. This quantification depends on the local spatial distribution of fission products in the used fuel matrix. This information is also important in fuel performance analysis.

In summary, the physicochemical phenomena involved in the dissolution of used fuel is very complex involving phase change in liquid, vapor, and solid phases. Heterogeneous and homogeneous, irreversible and reversible reactions in all phases need to be carefully considered for proper quantitative analysis. Furthermore, since industrial systems require high throughput of materials, a continuous, non-equilibrium, material flow is a common process choice which demands the understanding of transport in convecting media for open systems. Coupled with chemical thermomechanics, there is also the concern of nuclear critically safety which may require a combined neutron transport study.

3 System description

As previously mentioned the system of interest is the dissolver in a dissolver/digestor station. Prototype rotary dissolvers have been examined and operated in the past at the ORNL IET facility. A computer aided design (CAD) graphical model (fig. 3.1,

appendix A) of a rotary dissolver was developed here (guided by Odom and Kunselman, 1973; Yarbro, 1980) to approximate a dissolver prototype operated at ORNL in the past (Burch et al., 1977, p. 4-13). By virtue of a rigid body motion analysis of the CAD model, new features were introduced in the design, and insight in the mechanics of the operation was obtained to derive a consistent plant-level (reduced) model. In particular, geometric insight on solid/liquid backmixing, frontmixing, and solid transfer timing schedule was obtained without either a physical device being built or available. The CAD rigid motion is essential for developing a satisfactory model for the solid transfer mechanism which could be further improved via simulation of the solid transfer granular flow; a simulation currently within reach of high-performance computing.

In this equipment, an elongated drum with its axis slightly inclined (3° to 14°) relative to the horizontal direction is divided into radial compartments separated by partitions (figs. 3.1 and A.1). The compartment partitions are perforated with concentric slots at a short distance from the outer rim of the drum to allow liquid to flow by gravity from one compartment at higher elevation to the next at a lower elevation (figs. 3.2 and A.2). A pool of liquid is retained at the bottom of each compartment with ideal depth equal to the distance from the drum wall to the slot perforations (rotation will disturb the ideal pool depth). For the design evaluated here (fig. 3.1 and appendix A) the liquid pool inside each compartment is estimated as 10.3 L. A subscale computational fluid mechanics simulation could make this estimate rigorous and provide time/parameter variations for this quantity. Liquid overflows through the slots from one compartment to the next as the drum rotates (fig. 3.2).

Each compartment partition has a perforated baffle which rotates with the drum lifting solids from the liquid pool and dropping them back into the liquid flowing stream as the baffle completes each revolution (indicated by large arrows in fig. 3.2). In this mixing-leaching rotation mode, each compartment has an initial amount of solids that dissolves into the continuously flowing liquid stream. If solids dissolve to a sufficiently small particle size they are carried downstream with the flow as entrained particles. Otherwise, after a pre-specified residence time is reached, the remaining solids must be transferred to the next compartment at a higher elevation. The transfer will expose the solids to a higher acid concentration inside the next compartment and allow further dissolution. Similarly, the compartment from which the solids were transferred receives solids from a lower acid concentration stage, hence providing a new level of dissolution strength for the incoming solids.

The transfer of solids against gravity is enabled by the joint action of the perforated baffles and their attached perforated chutes when rotated in the reverse direction. With the exception of the baffle in the discharge partition (fig. A.8), each baffle is the extension of a chute in the form of a conical perforated frustum that wraps around a central opening (figs. 3.2 and A.2). This opening has the shape of a concentric

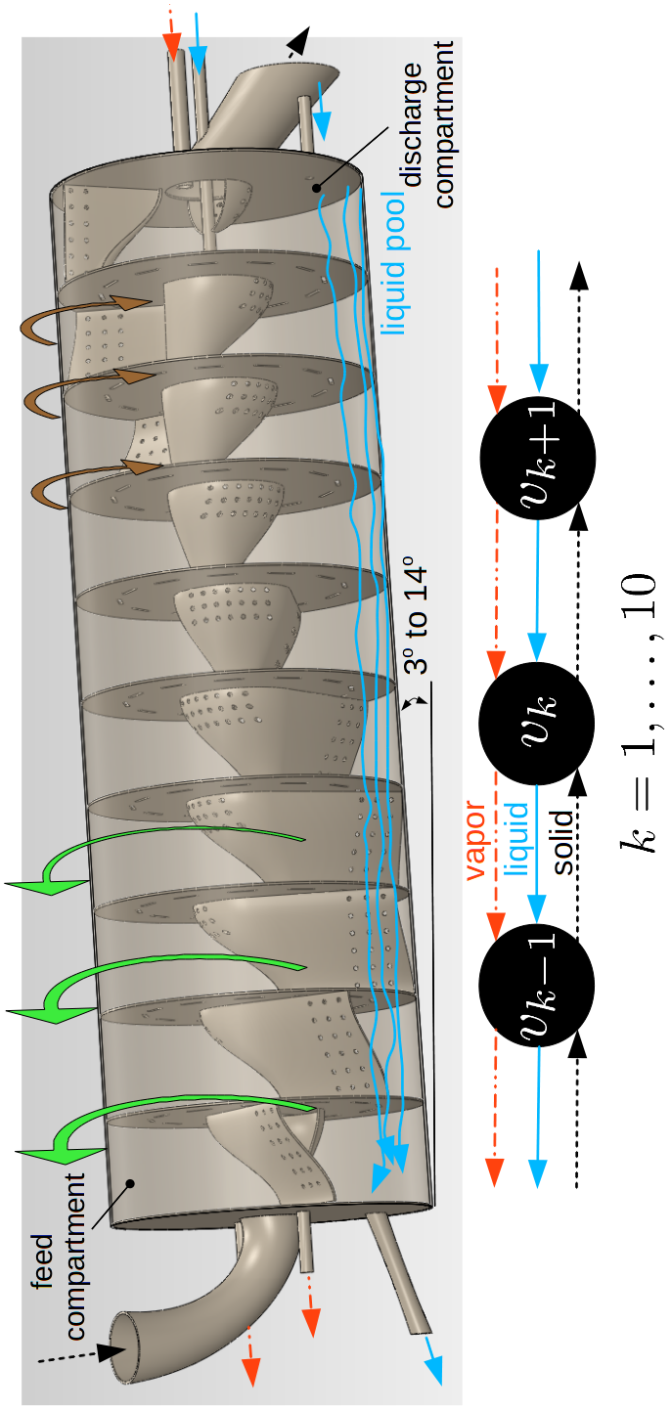

Fig. 3.1: *Continuous rotary dissolver CAD model for a* $1\,\mathrm{t\,d^{-1}}$ *dissolution capacity and its ten-stage, counter-current network plant-level graph (de Almeida, 2011). Under the mixing–leaching mode the drum rotates in the direction of the bigger arrows. Under this mode, the solids are held in each compartment and mixed in and out of the dissolving solution via the lifting action of the perforated baffles. At every* 20 min *the drum performs about one revolution in the opposite direction (smaller arrows) causing the baffles to scoop the solids from the bottom of the compartment and to slide them into the chute; this allows for the transfer of solids to the next (left to right) compartment. The last compartment on the right discharges the undissolved solids.*

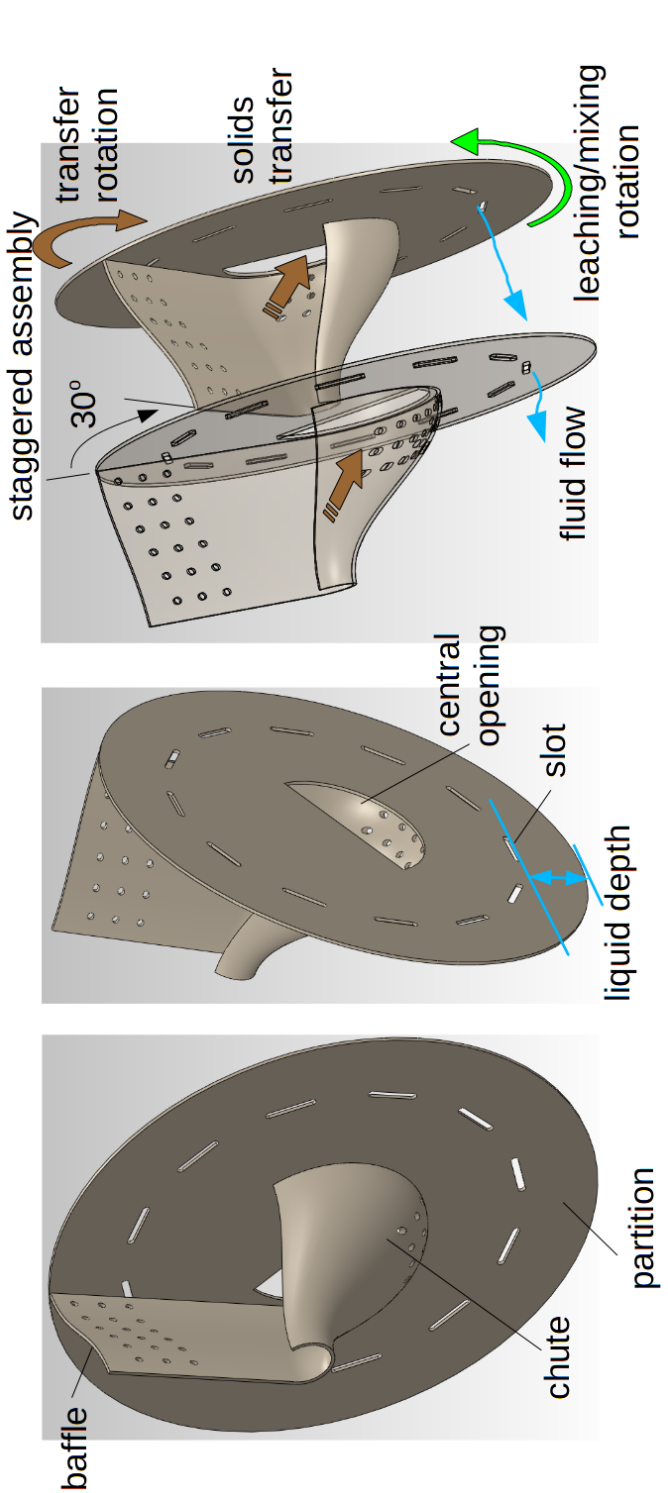

Fig. 3.2: *Rotary dissolver partition chute. The countercurrent flow of solids and liquid is enabled by the geometry and operation of the partition chutes. Here the partition baffles are staggered by* 30°. *A transfer (reverse) rotation mode uses the baffles to pick up solids from the bottom of the liquid pool and slide them into the chute through the central opening to the next compartment. The liquid depth depicted here implies an estimated liquid pool of* 10.3 L *in each compartment.*

half circle positioned with its diameter edge 30° relative to the horizontal direction when the baffle is at the top dead center (TDC, fig. A.2). The opening stays above the liquid level at all times to allow for transferring solids from one compartment to the next. By inspection of the resulting baffle-chute-opening geometry, it can be observed that a reverse rotation (figs. 3.2) will collect the solids at the bottom dead center (BDC) and slide them into the chute toward the central opening; this action transfers the solids against gravity into the next compartment.

The successful transfer of solids across compartments is one that minimizes solid backmixing and frontmixing; it depends on two conditions. First, the partitions need to be properly staggered. Second, the reverse rotation must be synchronized. The staggered geometry is needed to allow for an ordered transfer of solids, that is, a compartment at a higher elevation must transfer its solids before new solids are received from its neighbor at lower elevation. Hence the order of transfer is such that the discharge compartment transfers first and the feed compartment, last (fig. A.1). The discharge compartment consists of the region formed by the discharge partition and the discharge head (figs. A.6,A.7, A.8), similarly the feed compartment is formed by the feed and feed head counterparts (figs. A.3,A.4, A.5).

A rigid body motion of the CAD model shows that with the discharge baffle at TDC, the feed baffle needs to be installed at $\pi/2$ angle. Hence all remaining partition baffles should be equally distributed in the remaining $3\pi/2$ angle, for best weight balance in the drum, starting from the feed partition baffle and proceeding toward the discharge baffle (fig. A.1). Since here we have used eight additional partition baffles, each one should be staggered by 30° (*i.e.*, $3\pi/2$ divided into nine arcs).

The drum rotation is slow ($\approx$ 1 to 2 rpm) to reduce wear of the surface of the drum's internal wall by virtue of collision with the solids. The residence time of the solids during the mixing-leaching rotation mode could be 20 min, depending on the desired throughput. The synchronization for the solids transfer must start with the discharge baffle at TDC. At this point, all solids in the discharge compartment are at the bottom, and all the solids at the feed compartment are lifted and held on the perforated baffle in the horizontal position (note staggering of the feed baffle relative to the discharge baffle described in the foregoing). The drum must be rotated in reverse mode at the moment the discharge baffle reaches TDC for one full revolution. This will discharge all solids previously stored in the discharge compartment that were undergoing leaching. Since the discharge neighbor compartment's baffle is staggered by 30°, it will be in position to start feeding new solids into the discharge compartment before one full revolution of the discharge baffle. A similar geometric positioning occurs for all other compartments, that is, all compartments start receiving solids before the end of their outbound solid transfer process. This simultaneous movement of solids in and out of every compartment occurs without any solid backmixing (or frontmixing) if carried out perfectly. In practice some amount of solids may either

backmix or frontmix.

The feed compartment is the last to transfer solids, and in view of the staggered arrangement it will not reach TDC until the reverse rotation of the drum reaches 1.75 rotations (or $7\pi/4$). This is as far as the reverse rotation can go without causing the discharge compartment to start discharging the newly received solids (frontmixing); a situation that must be avoided. This amount of rotation is also all it is needed to completely empty the feed compartment. At either this point ($7\pi/4$ reverse rotation) or 90° sooner, the feed compartment is ready to receive fresh sheared fuel solids. Every compartment will transfer and receive solids simultaneously for up to 60° reverse rotation without backmixing. In a 1 rpm rotation rate this entails a transfer time overlap of 10 s.

In summary, at 1 rpm rotation rate, the total transfer of solids in/out any compartment takes 120° or 20 s, wherein during 60°, or 10 s, there is simultaneous inflow and outflow of solids without backmixing or frontmixing. It takes a total of 90° or 15 s to transfer solids out of the compartment and the same amount of time to transfer solids into the compartment.

The foregoing timing is based on an ideal movement of granular material following a rigid body motion of the rotary dissolver. In practice, there will be departure from ideality causing solids to either backmix or frontmix. However it is expected that these adverse effects will be mitigated by closely following an appropriate rotation schedule. Likewise, backmixing in the liquid phase is likely to occur in view of the adverse liquid mass density gradient in the axial direction; heavier liquid tends to stay at the lower end of the dissolver. This tendency is balanced by the presence of perforations on the baffles and the partition slots (suggested by fluid flow visualization, Yarbro, 1980). Here computational fluid mechanics could be instrumental in verifying these assumptions and/or helping design appropriate perforations.

A dissolver exchanges material streams continuously with its connected components (fig. 3.3), except for the loading of solids from either the chopper or the voloxidizer which may feed solids in a cyclic form.

4 Mathematical model

The rotary dissolver, described in the previous section, is a phase-contacting device which can be abstracted into a linear countercurrent cascade network (de Almeida, 2011). Initial information about the system has been provided to allow for the construction of a simple network (fig. 3.1) induced by the natural compartment structured of the rotary dissolver. Therefore, vertices in the network are assigned to the physical region between partitions in the dissolver drum. It entails the vertex set $\{v_k,\ k = 1, \ldots, 10\}$ with multiple directed edges representing the flow of solids, liq-

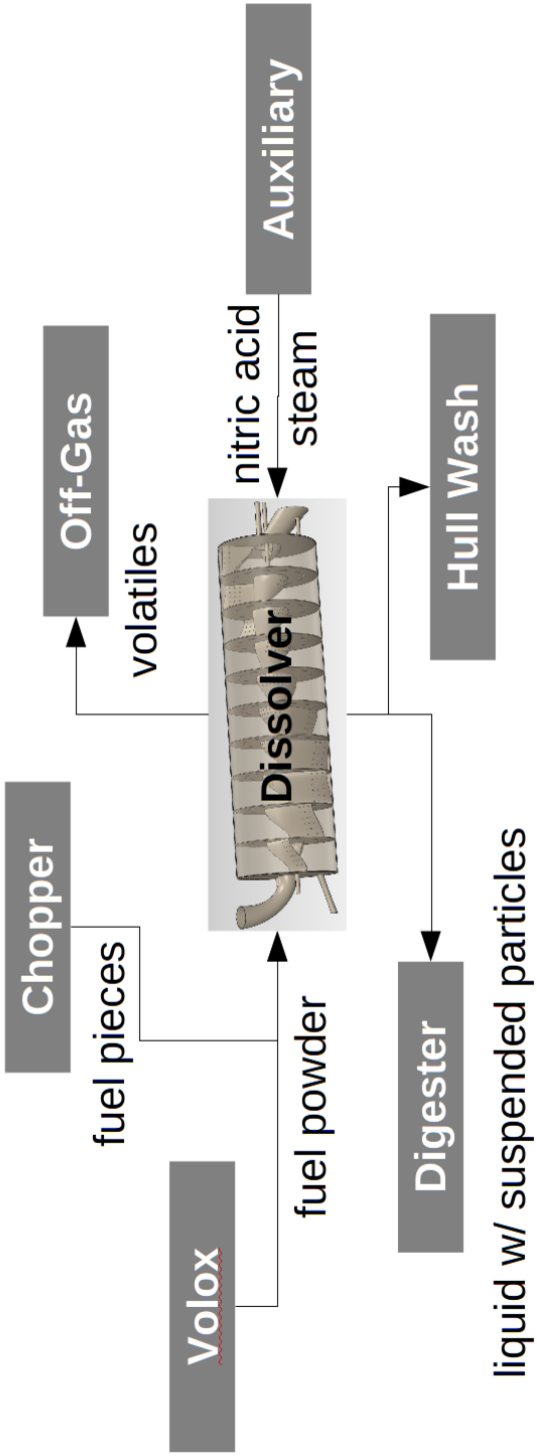

Fig. 3.3: *Rotary dissolver connectivity. Continuous streams flow in and out of the dissolver except for the solids feed which may need to be cyclic.*

uid, and vapor in each vertex.

This network representation is obviously not unique and can certainly be elaborated to include additional structure. In particular, vertices could be added to represent the partition chute domain, allowing for more realistic consideration of the finite-time solid transfer operation.

A non-equilibrium network transport balance approach is followed here. Once a graph of the contacting operation is defined, and the system operation identified, it remains the job of postulating the laws that govern the macroscopic transport of material in the network. A network theory based on the underlying continuum chemical thermomechanics was initiated in a preceding report which is followed in the next sections (notation as in the cited reference).

The charge of solids (here taken as a batch of uniform-size spheres) in the feed compartment, and the solids transfer in each compartment, are considered instantaneous for the sake of simplicity. This leads to a change in the volume of solids in each network vertex at the transfer time. One way to accommodate this time-dependent cycle is to impose a periodic initial condition for the system of governing equations. That is, the time interval of interest for the evolution of the system

$$I := \{t \in \mathbb{P} \mid 0 \leq t \leq T\}$$

is segmented into $n_{\text{trf}}\, T_{\text{trf}}$ segments where T_{trf} is the time period for the mixing-leaching rotation mode, and n_{trf} is the total number of transfers. That is, no solids transfer occur between $n_{\text{trf}}\, T_{\text{trf}}$ and $(n_{\text{trf}} + 1)\, T_{\text{trf}}$; typically $T_{\text{trf}} = 20\,\text{min}$. This segmentation allows for the conventional time integration of a coupled system of differential equations using an initial condition obtained from the end of the previous time segment, modified by the new values of the solid volume in each compartment due to the solid transfer, and new solid charge in the feed compartment. Additional details on this is give in section 4.3.

The dissolver (sec. 3), contains ten compartments, therefore $n_{\text{trf}} \geq 10$ will be needed to move the solids into the discharge compartment depending on the operating parameters. In practice more transfers than the number of compartments are needed in view of the dissolution transient where particles get fully dissolved before reaching the discharge. Since only pellets are used for this modeling exercise, parameters for the model are selected so that the pellets reduce to the size of $\leq 100\,\mu\text{m}$-diameter particles as the dissolver reaches fully developed conditions. In this case it is assumed that the particles are fully entrained into the liquid and flow with the product stream; this represents a complete dissolution operation.

4.1 Mass balance

A vertex-wise mass balance for the liquid phase ℓ on the kth vertex with material flow from its neighbors results in

$$d_t\big(\rho_{a,\ell}^{(k)}\, V_\ell^{(k)}\big) = \sum_{j\neq k} \rho_{a,\ell}^{(k)}\, f_\ell^{(\overrightarrow{k,j})} + \mathscr{M}_{a,\ell}^{(k)} \qquad \forall \quad k = 1,\ldots,N_{\mathrm{v}}, \quad \text{and} \quad a = 1,\ldots,\mathscr{A}_\ell^{(k)}. \tag{4.1}$$

For the particular linear network of vertices used in the current model, the summation in (4.1) can be simply expressed as

$$\sum_{j\neq k} \rho_{a,\ell}^{(k)}\, f_\ell^{(\overrightarrow{k,j})} =: -\rho_{a,\ell}^{(k)}\, f_\ell^{(k)} + \rho_{a,\ell}^{(k+1)}\, f_\ell^{(k+1)}.$$

Where $f_\ell^{(k)} \geq 0$ is the volumetric flow rate leaving the kth vertex stage and $f_\ell^{(k+1)} \geq 0$ is the corresponding flow entering the stage. Here the number of vertices is $N_{\mathrm{v}} = 10$, backmixing and frontmixing terms have been neglected (de Almeida, 2011, (5.3)), the number of species in the liquid phase is $\mathscr{A}_\ell^{(k)} = 5$, with mass concentration for each specie denoted as $\rho_{\mathrm{H_2O}}^{(k)}$, $\rho_{\mathrm{HNO_3}}^{(k)}$, $\rho_{\mathrm{UO_2(NO_3)_2}}^{(k)}$, $\rho_{\mathrm{Pu(NO_3)_4}}^{(k)}$, and $\rho_{\mathrm{FP(NO_3)_{2.36}}}^{(k)}$, respectively, for every vertex; the last specie is a fictitious oxide representation of all fission products (Lewis, 1984).

The source/sink terms $\mathscr{M}_{a,\ell}^{(k)}$ are considerably complex in a more realistic model that accounts for the underlying sub-scale continuum transport. A path for an improved network model incorporating source/sink terms derived from volume-averaging the continuum-scale equations has been proposed in a previous report, which will require a theory and modeling program in the future. For the present purpose of this communication, the source and sink terms are derived by empirical overall rate kinetics (Uriarte and Rainey, 1965), and empirical overall mass-action reaction mechanisms (Lewis, 1984). In addition, in view of the injection of the acid feed stream in the penultimate compartment (fig. A.8), $\mathscr{M}_{a,\ell}^{(9)}$ must account for the water and nitric acid sources; this is described later.

A similar mass balance for the solid phase need only to consider, for this approximate model, the conservation of the total solid mass in each stage vertex

$$\rho_s^{(k)}\, d_t V_s^{(k)} = \mathscr{M}_s^{(k)} \qquad \forall \quad k = 1,\ldots,N_{\mathrm{v}}, \tag{4.2}$$

where $\mathscr{M}_s^{(k)}$ represents the dissolution rate of the solid phase within the kth stage vertex with the assumption that the solid mass density $\rho_s^{(k)}$ is a constant.

The present modeling approach neglects the governing equations representing the principles of power balance, energy balance, and entropy imbalance (de Almeida, 2011, sec. 5.2) for all phases. In addition, the vapor phase is ignored. These assumptions are equivalent to considering all stages in mechanical and thermal equilibrium. An important aspect of this modeling exercise is to acknowledge the approximations made and the path forward for improving the realism of the model.

At this point, the model involves 14 thermomechanical variables in equations (4.1)–(4.2) which define a chemical thermomechanical process represented by 2 lists of functions $(\cdot)\colon I_i \to \mathbb{R}$

$$\mathcal{P}_\ell^{(k)} := \big(\rho_{a,\ell}^{(k)},\ V_\ell^{(k)},\ f_\ell^{(k)},\ \mathscr{M}_{a,\ell}^{(k)}\big) \quad \forall\ a = 1,\dots,5,\ \text{and} \tag{4.3}$$

$$\mathcal{P}_s^{(k)} := \big(V_s^{(k)},\ \mathscr{M}_s^{(k)}\big), \tag{4.4}$$

where $I_i := \{t \in \mathbb{P} \mid i\,T_{\text{trf}} \le t \le (i+1)\,T_{\text{trf}}\}\ \forall\ i \in n_{\text{trf}}^{]}$ is the time segment for the ith solid transfer. Since only 6 equations per stage are available, 8 additional equations are needed for a solvable system. This is the goal of a constitutive theory which is described next.

4.2 Constitutive restrictions

A constitutive theory defines additional equations that make the basic balance equations solvable. This is accomplished by introducing equations that specializes the balance equations to a class of materials or to a system behavior. To this end, a set of independent variables is assumed (the use of the stage vertex superscript (k) is discontinued in this section)

$$\big\{\rho_{a,\ell}, V_\ell, V_s,\big\} \quad \forall \quad a = 1,\dots,5, \tag{4.5}$$

which defines a (thermo)kinetic process in the time interval $I_i\ \forall\ i \in n_{\text{trf}}^{]}$. A vast number of processes (4.3)–(4.4) exist for thermomechanical functions compatible with the mass balance equations. To determine a particular process, it is sufficient to provide constitutive relations for 7 constitutive variables

$$\Upsilon_\ell := \big(f_\ell,\ \mathscr{M}_{a,\ell}\big) \quad \forall \quad a = 1,\dots,5,\ \text{and}$$
$$\Upsilon_s := \big(\mathscr{M}_s\big).$$

Application of the principle of determinism and time-shift allows the representation of the above constitutive variables as response functions of the thermokinetic variables (de Almeida, 2011, sec. 5.3)

$$\Upsilon_\ell(t) = \mathscr{G}_\ell\big(\rho_{a,\ell}(t),\ d_t\rho_{a,\ell},\ V_\ell(t),\ d_tV_\ell,\ V_s(t),\ d_tV_s\big) \quad \forall \quad a = 1,\dots,5, \tag{4.6}$$

$$\Upsilon_s(t) = \mathscr{G}_s\big(\rho_{a,\ell}(t),\ d_t\rho_{a,\ell},\ V_\ell(t),\ d_tV_\ell,\ V_s(t),\ d_tV_s\big) \quad \forall \quad a = 1,\dots,5. \tag{4.7}$$

In the next sections, explicit forms of response functions will be derived following the form of (4.6)–(4.7).

4.2.1 Heterogeneous solid dissolution kinetics

An empirical overall dissolution rate of the solid phase in the kth stage is used for defining the response function (4.7) assumed to be of the form of a rate law

$$\mathscr{M}_s^{(k)}(t) := -k_s^{(k)} \left(c_{\mathrm{HNO_3}}^{(k)}\right)^m f\, A_s^{(k)}(t) \qquad \forall \quad k = 1, \ldots, 10, \tag{4.8}$$

with rate constant of dissociation $k_s^{(k)}$, reaction order m, molar concentration (molarity) of HNO_3, solid surface roughness factor f, and solid surface area exposed to the liquid phase $A_s^{(k)}$. Uriarte and Rainey (1965) warns the user of (4.8) about the difficulty of obtaining experimental values for these parameters which can lead to errors in dissolution rates up to 50%, primarily due to the difficulty of reliably measuring the surface area of the dissolved solid. This is particularly difficult at later times of dissolution when roughness has developed on the surface of the solid.

The reaction order is defined as $m := 2\,(2 - x_{\mathrm{UO_2}})$ where $x_{\mathrm{UO_2}}$ is the molar fraction of UO_2 in the solid pellet. The empirical rate constant of dissociation in the kth stage is defined as (Uriarte and Rainey, 1965)

$$k_{\mathrm{s}}^{(k)} := \Big(0.48\, \exp\left(-0.091 \rho_{\mathrm{s}}'\right)\Big)^{x_{\mathrm{UO_2}}} \Big(5\, \exp\left(-0.27 \rho_{\mathrm{s}}'\right)\Big)^{(1 - x_{\mathrm{UO_2}})}, \tag{4.9}$$

where ρ' is the percent mass density of the solid in units of ideal mass density

$$\rho_{\mathrm{s}}' := \frac{100\, \rho_{\mathrm{s}}}{x_{\mathrm{UO_2}} \rho_{\mathrm{UO_2}} + x_{\mathrm{PuO_2}} \rho_{\mathrm{PuO_2}} + x_{\mathrm{FPO_{1.18}}} \rho_{\mathrm{FPO_{1.18}}}}. \tag{4.10}$$

In the above definition the mass densities of the pure compounds are used. Finally, the surface area of the solid exposed to the liquid phase is a function of the solid volume, $A_s^{(k)}(t) = g\big(V_s^{(k)}(t)\big)$, through a shape geometry function. Here a simple spherical geometry is used for the solid pellets. It is shown that the working response function (4.8) satisfies the form (4.7).

4.2.2 Overall reaction mechanisms

Empirically derived global mass-action reactions can be used to propose a response function for the constitutive variables $\mathscr{M}_{a,\ell}$. An overall mechanism used by Lewis

(1984) when $c_{\mathrm{HNO_3}} \leq 8\,\mathrm{M}$ is

$$\mathrm{UO_{2(s)}} + 2.7\,\mathrm{HNO_3} \xrightarrow{100\,^{\circ}\mathrm{C}} \mathrm{UO_2(NO_3)_2} + 0.7\,\mathrm{NO_{(g)}} + 1.3\,\mathrm{H_2O_{(aq)}}, \tag{4.11}$$

$$\mathrm{PuO_{2(s)}} + 4\,\mathrm{HNO_3} \xrightarrow{100\,^{\circ}\mathrm{C}} \mathrm{Pu(NO_3)_4} + 2\,\mathrm{H_2O_{(aq)}}, \text{ and} \tag{4.12}$$

$$\mathrm{FPO_{1.18(s)}} + 2.36\,\mathrm{HNO_3} \xrightarrow{100\,^{\circ}\mathrm{C}} \mathrm{FP(NO_3)_{2.36}} + 1.18\,\mathrm{H_2O_{(aq)}}. \tag{4.13}$$

Based on this mechanism, the instantaneous source of water in the kth stage vertex is defined as

$$\boxed{\mathscr{M}^{(k)}_{\mathrm{H_2O},\ell}(t) := \left(1.3\,\dot{n}^{(k)}_{\mathrm{UO_2}} + 2\,\dot{n}^{(k)}_{\mathrm{PuO_2}} + 1.18\,\dot{n}^{(k)}_{\mathrm{FPO_{1.18}}}\right) M_{\mathrm{H_2O}}} \tag{4.14}$$

where the dissolution mole rate for each solid specie in the kth stage vertex is obtained from

$$\dot{n}^{(k)}_i(t) = \frac{|\mathscr{M}^{(k)}_s(t)|\,w_i}{M_i}, \quad i \text{ denotes } \mathrm{UO_2}, \mathrm{PuO_2}, \text{and } \mathrm{FPO_{1.18}}, \tag{4.15}$$

with M_i representing the molar mass of the solid species, and w_i, the corresponding mass fraction; the latter is known from the composition of the fuel and considered a constant. The molar mass of water, $M_{\mathrm{H_2O}}$, is used to convert water moles produced by the dissolution reactions into mass. An additional source of water exists for the penultimate compartment ($k = 9$) where the acid feed is delivered. Hence, the following source term need to be added to (4.14): $\mathscr{F}^{(9)}_\ell \mathscr{C}^{(9)}_{\mathrm{H_2O}} M_{\mathrm{H_2O}}$.

Similarly, the consumption of nitric acid is computed from the response function

$$\boxed{\mathscr{M}^{(k)}_{\mathrm{HNO_3},\ell}(t) := -\left(2.7\,\dot{n}^{(k)}_{\mathrm{UO_2}} + 4\,\dot{n}^{(k)}_{\mathrm{PuO_2}} + 2.36\,\dot{n}^{(k)}_{\mathrm{FPO_{1.18}}}\right) M_{\mathrm{HNO_3}},} \tag{4.16}$$

with an additional source term in the penultimate compartment: $\mathscr{F}^{(9)}_\ell \mathscr{C}^{(9)}_{\mathrm{HNO_3}} M_{\mathrm{HNO_3}}$ which must be added to (4.16). The production of uranyl nitrate is computed from the response function

$$\boxed{\mathscr{M}^{(k)}_{\mathrm{UO_2(NO_3)_2},\ell}(t) := 1.0\,\dot{n}^{(k)}_{\mathrm{UO_2}}\,M_{\mathrm{UO_2(NO_3)_2}}.} \tag{4.17}$$

The production of plutonium nitrate is computed from the response function

$$\boxed{\mathscr{M}^{(k)}_{\mathrm{Pu(NO_3)_4},\ell}(t) := 1.0\,\dot{n}^{(k)}_{\mathrm{PuO_2}}\,M_{\mathrm{Pu(NO_3)_4}}.} \tag{4.18}$$

Finally, the production of fission product nitrates is computed from the response function

$$\boxed{\mathscr{M}^{(k)}_{\mathrm{FP(NO_3)_{2.36}},\ell}(t) := 1.0\,\dot{n}^{(k)}_{\mathrm{FPO_{1.18}}}\,M_{\mathrm{FP(NO_3)_{2.36}}}.} \tag{4.19}$$

Note that the sum of the mass sources/sink in the liquid phase do not necessarily add to zero $\sum_a \mathscr{M}_{a,\ell}^{(k)} \neq 0 \; \forall \; k$.

The reaction mechanism (4.11)–(4.13) needs modification when using higher acid strengths $c_{\mathrm{HNO_3}} > 8\,\mathrm{M}$ by replacing (4.11) with

$$\mathrm{UO_{2(s)}} + 4\,\mathrm{HNO_3} \longrightarrow \mathrm{UO_2(NO_3)_2} + 2\,\mathrm{NO_{2(g)}} + 2\,\mathrm{H_2O_{(aq)}}.$$

In addition if the fuel has been oxidized, as in a voloxidation pretreatment, (4.11) and (4.13) need to be replaced with the approximations (Lewis, 1984)

$$\begin{aligned} \mathrm{U_3O_{8(s)}} + 7.35\,\mathrm{HNO_3} &\longrightarrow 3\,\mathrm{UO_2(NO_3)_2} + \mathrm{NO_{2(g)}} + 0.35\,\mathrm{NO} + 3.65\,\mathrm{H_2O_{(aq)}}, \text{ and} \\ \mathrm{FPO_{1.7(s)}} + 3.39\,\mathrm{HNO_3} &\longrightarrow \mathrm{FP(NO_3)_{3.39}} + 1.7\,\mathrm{H_2O_{(aq)}}. \end{aligned}$$

These empirical reaction mechanisms have been augmented in more recent years (Fukasawa et al., 1991; Homma et al., 1993; Ikeda et al., 1995, 1999; Yasuike et al., 1995; Zhao and Chen, 2008a,b) which could be used to compare various alternative formulations. However, it remains largely untested the performance of the resulting models when comparing plant-level modeling predictions to experimental results. For the purpose of this report, describing the formalism of deriving a rational plant-level model is more important than trying to incorporate specific reaction mechanisms; these can be accommodated in the future.

4.2.3 Volume constraints

The previous sections (sub-sec. 4.2.1 and 4.2.2) described the basic constitutive aspects of the network dissolver model which added the constitutive equations (4.8) and (4.14)–(4.19) to the basic network governing equations set (4.1) and (4.2). The total is now 12, hence an additional 2 equations are needed for a solvable system containing the 14 thermomechanical variables (4.3)–(4.4).

On the theoretical side, what is still missing in the mathematical description of material behavior is an account of volume changes for the class of fluids and solids involved in the application. Since the mass density of the solid phase is considered constant, *i.e.* the solid is incompressible, the volume change of the solid phase is accounted for in (4.2) in conjunction with a constant value for $\rho_s^{(k)}$. Hence the job at hand is to quantify volume changes in the liquid phase (the gas phase has been neglected in this development). There are two components for the change of volume in a network k-stage vertex, $V_\ell^{(k)}$, namely, change by creation of species, and change by convection of material to and from the stage in view of the holdup capacity inherent in each digestor compartment. The former is a change of chemical nature, the latter,

a change of mechanical fluid flow. These considerations will generate the remaining 2 constitutive equations needed to close the model.

Volume constraints are internal constraints in a constitutive theory (de Almeida, 2011, sec. 5.3.1) and they should be treated as a condition that produces no work and no entropy. This aspect of the theory has not been investigated here and remains to be done in the future.

4.2.4 Species partial molar volume

As chemical species are formed near the solid-liquid interface a change in volume of the liquid phase results. This molecular phenomenon is instantaneous relative to the time scale of the dissolution of a pellet and the revolution time of the digestor. Therefore, a thermodynamical equilibrium assumption for this particular aspect is acceptable at this point. The volume of the liquid phase in the kth network vertex is then a function of the molar fraction, x_a, and partial molar volumes of the solutes

$$V_\ell^{(k)}(t) = \sum_{a=1}^{5} x_a^{(k)}(t)\, \overline{V}_a \quad \text{where} \quad \overline{V}_a := \left(\partial_{x_a} V\right)_{P,T,x_b \neq a}.$$

The partial molar volumes of all species, $\left(\partial_{x_a} V\right)_{P,T,x_b \neq a}$ is a thermodynamic property at constant temperature T and pressure P obtained either from tabulated experimental data or an off-line thermodynamic simulation, say via equilibrium molecular dynamics. Another form of expressing the previous constitutive restriction is in the form of a mass density constraint for the liquid mixture

$$\boxed{\rho_\ell^{(k)}(t) := \sum_{a=1}^{5} \rho_{a,\ell}^{(k)} = R(T, P, x_{a=1,\ldots,5}), \qquad (4.20)}$$

which is in the response function form anticipated in (4.6). This constitutive equation augments the basic set by enforcing a particular material behavior. In particular, it accounts for non-ideality of the liquid mixture from a thermodynamics stand point. A restricted empirical form of (4.20) was used from (Lewis, 1984) which does not account for the partial molar volume of the fission products. Future work could use off-line large-scale molecular dynamics simulations to map the function $R\colon (T, P, x_{a=1,\ldots,5}) \in \mathbb{P} \times \mathbb{P} \times \mathbb{P}^5 \to \mathbb{P}$ function for solutes of interest to the dissolution of nuclear materials.

4.2.5 Volumetric flow capacity function

A second mechanism of volume variation in the liquid phase is the variable flow capacity of each digester compartment. A direct flow balance for each k-stage, ignoring

the effects of hydrodynamic backmixing/frontmixing, leads to

$$\boxed{d_t V_\ell^{(k)} = -C\big(V_\ell^{(k)}, V_s^{(k)}, \Omega\big) + f_\ell^{(k+1)} + \mathscr{F}_\ell^{(k)}} \quad (4.21)$$

where the capacity function, $C\colon \big(V_\ell^{(k)}, V_s^{(k)}, \Omega\big) \in \mathbb{P} \times \mathbb{P} \times \mathbb{P} \to \mathbb{P}$, provides the volumetric flow rate of the exiting liquid phase as a function of the existing volumes of solid and liquid phases, and the rotation rate of the dissolver. This dependency is only a first approximation. Here a sub-scale off-line fluid flow simulation could provide a much more complete description of this function, justifying the need for large sub-scale simulations. An empirical power-law function was used in this work which relates flow rate to liquid phase volume (Lewis and Weber, 1980)

$$C(V_\ell^{(k)}, V_s^{(k)}, \Omega) := \begin{cases} \left(\frac{V_\ell^{(k)} + V_s^{(k)} - V_0}{G}\right)^p & \text{if} \quad V_\ell^{(k)} + V_s^{(k)} - V_0 > 0, \\ 0 & \text{otherwise.} \end{cases} \quad (4.22)$$

The volumetric flow rate source/sink $\mathscr{F}_\ell^{(k)}$ accounts for any injection or withdraw of liquid in the kth stage. The only place this source is used in the current dissolver prototype is in the penultimate compartment where the acid feed is introduced (fig. A.8).

4.3 Mathematical problem

A presentation of the equations in the form of a mathematical problem is in order to help define a solution strategy. By virtue of (4.15) all source functions in the liquid phase (4.14)–(4.19) are a function of the solid phase sink function (4.8). The latter is a function of the molarity of the nitric acid in the liquid phase. Therefore, upon substitution of (4.8) and (4.14)–(4.19) into the basic governing equations, (4.1) and (4.2), the mathematical problem can be stated as follows.

Find, for all transfer time segments $I_i \; \forall \; i \in n_{\text{trf}}^{\rfloor}$, the time-dependent functions

$(\cdot)\colon t \in I_i \to \mathbb{R}$

$$\rho_{a,\ell}^{(k)},\ V_\ell^{(k)},\ f_\ell^{(k)},\ V_s^{(k)},\ \text{for}\quad \forall\ a = 1,\dots,5,\ k = 1,\dots,10, \tag{4.23a}$$

satisfying the basic network equations

$$\rho_s^{(k)}\, d_t V_s^{(k)} = \mathscr{M}_s^{(k)},\ \text{and} \tag{4.23b}$$

$$d_t\big(\rho_{a,\ell}^{(k)}\ V_\ell^{(k)}\big) = -\rho_{a,\ell}^{(k)}\, f_\ell^{(k)} + \rho_{a,\ell}^{(k+1)}\, f_\ell^{(k+1)} + \mathscr{M}_{a,\ell}^{(k)}, \tag{4.23c}$$

and the constitutive equations

$$d_t V_\ell^{(k)} = -C\big(V_\ell^{(k)}, V_s^{(k)}, \Omega\big) + f_\ell^{(k+1)} + \mathscr{F}_\ell^{(k)},\ \text{and} \tag{4.23d}$$

$$\sum_{a=1}^{5} \rho_{a,\ell}^{(k)} = R(T, P, x_{a=1,\dots,5}), \tag{4.23e}$$

using the constitutive functions (4.8) and (4.14)–(4.19), and the constitutive thermodynamics, flow capacity functions, respectively $R(\cdot)$, and $C(\cdot)$, and the volumetric flow rate sources $\mathscr{F}_\ell^{(k)} = 0\ \forall\ k \neq 9$.

Equations (4.23b)–(4.23e) require initial conditions for the initial time of every transfer time segment. For the initial conditions at $t = 0$, *i.e.*, the first transfer time segment I_0,

$$\rho_{a,\ell}^{(k)}(0) = {}_0\rho_{a,\ell}^{(k)},\ V_\ell^{(k)}(0) = {}_0V_\ell^{(k)},\ f_\ell^{(k)}(0) = {}_0f_\ell^{(k)},\ V_s^{(k)}(0) = \mathscr{V}_s(0)$$
$$\forall\ a = 1,\dots,5,\quad \forall\ k = 1,\dots,10$$
$$\text{and}\qquad \rho_{a,\ell}^{(11)}(0) = {}_0\rho_{a,\ell}^{(11)},\ f_\ell^{(11)}(0) = {}_0f_\ell^{(11)} \tag{4.24}$$

The quantities on the right side of the equations (4.24) denote the data needed at the startup of the dissolver operation in this model. In particular, $V_s^{(1)}(0) = \mathscr{V}_s(0)$ is the volume of solids added instantaneously to the feed compartment at $t = 0$, while all other compartments have no solids, that is, $V_s^{(k)}(0) = 0\ \forall\ k \neq 1$. Note also that the data $\rho_{a,\ell}^{(11)}(0) = {}_0\rho_{a,\ell}^{(11)}$ and $f_\ell^{(11)}(0) = {}_0f_\ell^{(11)}$ represent the external flow into the rinse/discharge compartment; these can be a function of time. An additional feature of the dissolver initial condition is that the acid feed enters in the penultimate compartment (fig. A.8). Therefore the source $\mathscr{M}_{a,\ell}^{(9)}$ must include the addition of H_2O and HNO_3 from this feed stream with volumetric flow rate denoted $\mathscr{F}_\ell^{(9)}$.

Provided a solution to the mathematical problem (4.23)–(4.24) exists, the functions (4.23a) are determined in the first time segment $0 \le t \le T_{\text{trf}}$.

For the subsequent transfer times, $i \geq 1$, the initial conditions are derived from the functions (4.23a) evaluated at the end of the previous time segment, and the new solid charge to the feed compartment say, $\mathscr{V}_s(i\,T_{\text{trf}})$, which could vary with time depending on the upstream flow of solids from the fuel bundle chopper. In addition, the reverse drum rotation moves all solid content from one compartment to the next instantaneously, therefore the solid volume in each compartment at the end of each time segment is used as the initial value for the neighbor compartment. Mathematically, this is expressed for all transfer time segments, $I_i \;\forall\; i \geq 1$, in each network stage k as

$$\begin{aligned}
&\rho_{a,\ell}^{(k)}(i\,T_{\text{trf}}) = \rho_{a,\ell}^{(k)}\big((i-1)T_{\text{trf}}\big),\;\; V_\ell^{(k)}(i\,T_{\text{trf}}) = V_\ell^{(k)}\big((i-1)T_{\text{trf}}\big),\\
&\qquad\qquad f_\ell^{(k)}(i\,T_{\text{trf}}) = f_\ell^{(k)}\big((i-1)T_{\text{trf}}\big) \quad \forall\; a = 1,\ldots,5,\;\; k = 1,\ldots,10,\\
&V_s^{(1)}(i\,T_{\text{trf}}) = \mathscr{V}_s(i\,T_{\text{trf}}),\;\; V_s^{(k)}(i\,T_{\text{trf}}) = V_s^{(k-1)}\big((i-1)T_{\text{trf}}\big) \quad \forall\; k = 2,\ldots,10. \qquad (4.25)
\end{aligned}$$

Here the charge of solids in the feed compartment, $\mathscr{V}_s(t)$, is a piecewise function of time (possibly random, see fig. 6.1) since upstream variations in solid input are very likely to occur in practice. In addition, (4.25) assumes that the external liquid flow rate in the rinse/discharge compartment is a constant $f_\ell^{(11)}(i\,T_{\text{trf}}) = {}_0f_\ell^{(11)}$, and the acid feed in the penultimate compartment is time-dependent, that is, the parameters $\mathscr{F}_\ell^{(9)}(t)$, $\mathscr{C}_{\text{H}_2\text{O}}^{(9)}(t)$, and $\mathscr{C}_{\text{HNO}_3}^{(9)}(t)$ are functions of time.

One advantage of the time segmentation proposed here is that a time delay can be readily introduced to account for finite rates of transfer or feed. Moreover, a separate model, say at a smaller time-scale, could be coupled to predict details of the solids motion in the partition chutes. Such a model would make corrections to the values (4.25) at $t = (i-1)T_{\text{trf}}$ used as an initial condition for the ith transfer.

Finally, a solution to the problem (4.23)–(4.25) determines the functions (4.23a) for any time segment.

5 Data needed and provided

The network model proposed in section 4 requires parameters for the dissolution process and initial condition data for the mathematical problem. Parameters in tables 5.1, 5.2, and 5.3 were used for testing the solution method (see also sec. 8). Three parametric scenarios were explored using the same dissolver geometry (appendix A). First, a $0.5\,\text{t}\,\text{d}^{-1}$ capacity for dissolving breeder reactor fuel was tested. Second, the same fuel but a larger capacity, $1\,\text{t}\,\text{d}^{-1}$, was used. Last, a $1.7\,\text{t}\,\text{d}^{-1}$ capacity for used, light water reactor (LWR) fuel was designed for collaboration with a safeguards application (Cipiti and McDaniel, 2011; Cipiti et al., 2009).

Table 5.1: *Data for a breeder reactor used fuel.*

Quantity	Value	Description
ρ_s	$9.903\,\mathrm{g\,cm^{-3}}$	mass density of the solid pellets
$x_{\mathrm{UO_2}}$	0.737	mass fraction of UO_2 in the pellets
$x_{\mathrm{PuO_2}}$	0.211	mass fraction of PuO_2 in the pellets
$x_{\mathrm{FPO_{1.18}}}$	0.052	mass fraction of $FPO_{1.18}$ in the pellets
$\rho_{\mathrm{UO_2}}$	$8.3\,\mathrm{g\,cm^{-3}}$	mass density of UO_2
$\rho_{\mathrm{PuO_2}}$	$11.46\,\mathrm{g\,cm^{-3}}$	mass density of PuO_2
$\rho_{\mathrm{FPO_{1.18}}}$	$12.1\,\mathrm{g\,cm^{-3}}$	mass density of $FPO_{1.18}$

Different initial conditions can be used with this mathematical model. The initial conditions described in (4.24) assume a previously obtained fully developed liquid flow through the dissolver without any solids. This entails starting with an empty dissolver while feeding water to compartments 9 and 10. After the liquid holdup reaches steady state in each compartment, the concentration of nitric acid is increased to its nominal value and a steady state obtained (sec. 8). This liquid flow, with corresponding liquid holdup and concentrations is then used with solid pellets fed to compartment $k = 1$; this mimics the startup operation of a dissolver device in practice. The mathematical description of this startup process will not be provided at this time but some results are presented later (sec. 8).

In addition to the time-dependent functions (4.23a) obtained from solving the problem (4.23)–(4.25), many derived quantities of interest can be calculated, such as the total liquid product generated, total holdup in the dissolver device, total NO_x produced, and time needed for a statistical fully developed regime to be obtained; to name a few.

Table 5.2: *Data for breeder reactor used fuel dissolution at* $0.5\,\mathrm{t\,d^{-1}}$ *capacity.*

Quantity	Value	Description
T_{trf}	20 min	Solid transfer period
d_0	0.5 cm	Initial diameter of the pellets
$N_{\mathrm{p}}(0)$	10 983	Initial number of pellets
f	1	Solid surface roughness factor
g	$N_p\, 4\pi \left(\frac{3V_p}{4\pi}\right)^{2/3}$	Geometric function to compute the area of the solid phase given its volume
$f_\ell^{(11)}$	$0.4\,\mathrm{L/\,min}$	Volumetric liquid flow rate of the rinse stream to the discharge (rinse) compartment
$c_{\mathrm{HNO_3}}^{(11)}$	0 M	Nitric acid molarity in rinse feed stream in the last compartment
$\rho_{\mathrm{H_2O}}^{(11)}$	$971\,\mathrm{g\,L^{-1}}$	Water mass concentration in the feed stream to the discharge compartment
V_0	10.3 L	Yield volume parameter in the flow capacity function
p	2.7	Power-law exponent in the flow capacity function
G	0.201 941 L	Volume factor in the flow capacity function
$\mathscr{F}_\ell^{(9)}$	$1.5\,\mathrm{L/\,min}$	Volumetric liquid flow rate of the feed stream in the penultimate compartment ($k = 9$)
$\mathscr{C}_{\mathrm{HNO_3}}^{(9)}(0)$	8.9 M	Initial nitric acid molarity in the acid feed stream in the penultimate compartment
$\mathscr{C}_{\mathrm{H_2O}}^{(9)}(0)$	37.3 M	Initial water molarity in the acid feed stream in the penultimate compartment
$\rho_s \mathscr{V}_s(0)$	6.9 kg	Initial load of solids in the first compartment
T	108 °C	System's temperature

Table 5.3: *Data for breeder reactor used fuel dissolution at* $1\,\mathrm{t\,d^{-1}}$ *capacity. Other quantities as in table 5.2.*

Quantity	Value	Description
$N_\mathrm{p}(0)$	22 128	Initial number of pellets
$f_\ell^{(11)}$	$0.6\,\mathrm{L/\,min}$	Volumetric liquid flow rate of the rinse stream to the discharge (rinse) compartment
$\mathscr{F}_\ell^{(9)}$	$2\,\mathrm{L/\,min}$	Volumetric liquid flow rate of the feed stream in the penultimate compartment ($k = 9$)
$\mathscr{C}^{(9)}_{\mathrm{HNO_3}}(0)$	$10.4\,\mathrm{M}$	Initial nitric acid molarity in the acid feed stream in the penultimate compartment
$\mathscr{C}^{(9)}_{\mathrm{H_2O}}(0)$	$34.6\,\mathrm{M}$	Initial water molarity in the acid feed stream in the penultimate compartment
$\rho_s \mathscr{V}_s(0)$	$13.3\,\mathrm{kg}$	Initial load of solids in the first compartment

Table 5.4: *Data for LWR reactor used fuel dissolution at* $1.7\,\mathrm{t\,d^{-1}}$ *capacity. Other quantities as in tables 5.2–5.3.*

Quantity	Value	Description
$x_{\mathrm{UO_2}}$	0.96	mass fraction of UO_2 in the pellets
$x_{\mathrm{PuO_2}}$	0.02	mass fraction of PuO_2 in the pellets
$x_{\mathrm{FPO_{1.18}}}$	0.02	mass fraction of $FPO_{1.18}$ in the pellets
T_{trf}	20 min	Solid transfer period
d_0	1.1 cm	Initial diameter of the pellets
$N_{\mathrm{p}}(0)$	3728	Initial number of pellets
f	0.33	Solid surface roughness factor
$f_\ell^{(11)}$	2.0 L/ min	Volumetric liquid flow rate of the rinse stream to the discharge (rinse) compartment
V_0	21 L	Yield volume parameter in the flow capacity function
$\mathscr{F}_\ell^{(9)}$	3 L/ min	Volumetric liquid flow rate of the feed stream in the penultimate compartment ($k = 9$)
$\mathscr{C}^{(9)}_{\mathrm{HNO_3}}(0)$	9.7 M	Initial nitric acid molarity in the acid feed stream in the penultimate compartment
$\mathscr{C}^{(9)}_{\mathrm{H_2O}}(0)$	35.9 M	Initial water molarity in the acid feed stream in the penultimate compartment
$\rho_s \mathscr{V}_s(0)$	23 kg	Initial load of solids in the first compartment

6 Solution method and results

The problem (4.23) is an example of a system of differential algebraic equations (DAE) with index one. The algebraic equations (4.23e) represent a thermodynamic volume constraint. The volumetric outflow variables $f_\ell^{(k)}$ are referred to as the "algebraic" variables. The time segmentation approach in (4.23)–(4.25) allows for the direct use of robust DAE solvers. The advantages of using the the network model presented here have been extolled in de Almeida (2011, sec. 5.4). Of importance to this particular problem (4.23)–(4.25) is the ability of the DAE solver to implicitly solve the non-linear system of equations in a fully coupled manner with automatic time-adaptivity necessary for accurate calculation of the solid transfer cycles. Moreover, great savings in programing a computer code and explaining the solution method are made. The solution method information can be found in Brenan et al. (1996, DASPK: Differential Algebraic Solver with Sensitivity Analysis). Additional information on how to specify consistent initial conditions for the time derivatives of the unknowns will be presented in a future publication.

The following plots present typical results obtained from a numerical solution of the model. A future communication will describe the results and present an analysis of the problem. The results obtained here are relatively close to operational data. No attempt has been made to obtain reliable experimental data for validation, except for what is presented in section 8.

6.1 Breeder reactor fuel at $0.5\,\mathrm{t\,d^{-1}}$ dissolution capacity

Time variations in the results presented next are characterized by three time scales. First, the transfer period T_{trf}, second, the random variation of the solid transfer, captured here as a piecewise constant function, and last, a similar variation on the piecewise continuous function that approximates variations on the concentration of HNO_3 in the feed stream (fig. 6.1). Parameters for the present case are those presented in tables 5.1–5.2.

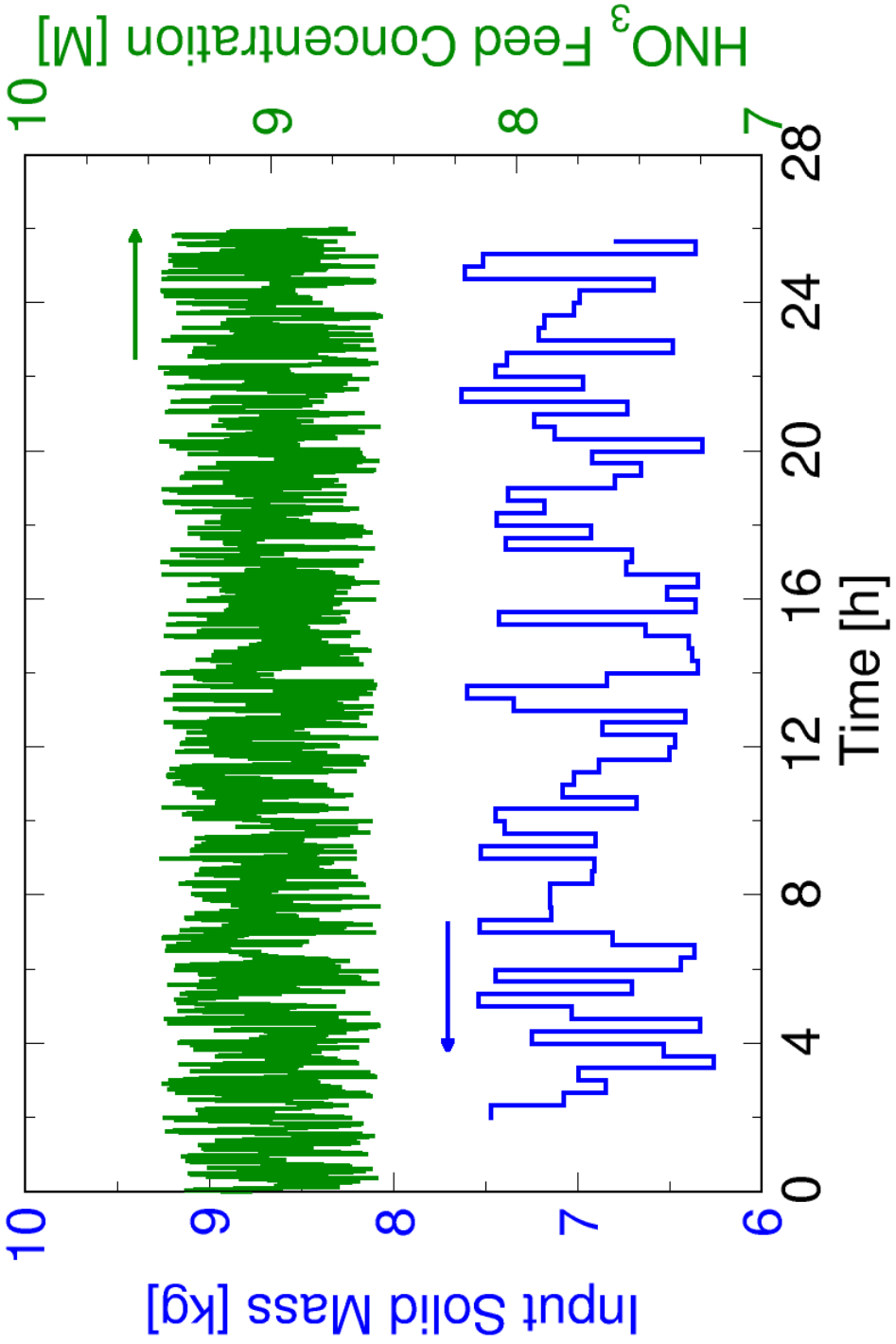

Fig. 6.1: ***Left ordinate axis:*** *Time variation of the mass of the solid loads in the first compartment inserted at each transfer period T_{trf}. This is a graphical representation of the piecewise constant, random function $\rho_s \mathscr{Y}_s(t)$ created by imposing a 10 % random variation around the mean 6.9 kg.* ***Right ordinate axis:*** *Input concentration of HNO_3 in the acid feed compartment ($k = 9$) with an imposed 20 % random variation around the mean 9 mol dm^{-3}. This is the graphical representation of the piecewise linear random function $\mathscr{C}^{(9)}_{\mathrm{HNO_3}}(t)$.*

6.1.1 Computed product stream characteristics

The product stream exits the first compartment of the dissolver and it provides the primary data for coupling the dissolution with downstream processes such as digestors, holding tanks, etc. Therefore various plots representing the the time variation of the predicted results are presented in this section.

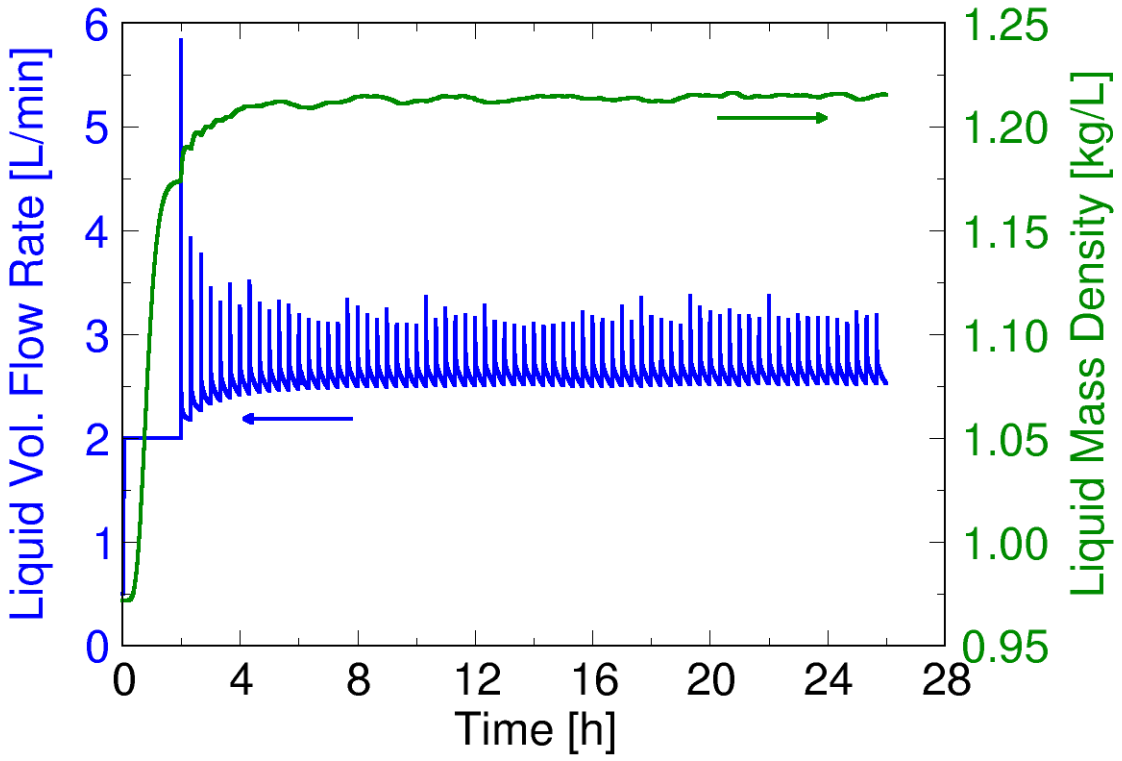

Fig. 6.2: ***Left ordinate axis:*** *Computed volumetric flow rate of the product stream.* ***Right ordinate axis:*** *Corresponding mass density. Capacity of* $0.5\,\mathrm{t\,d^{-1}}$.

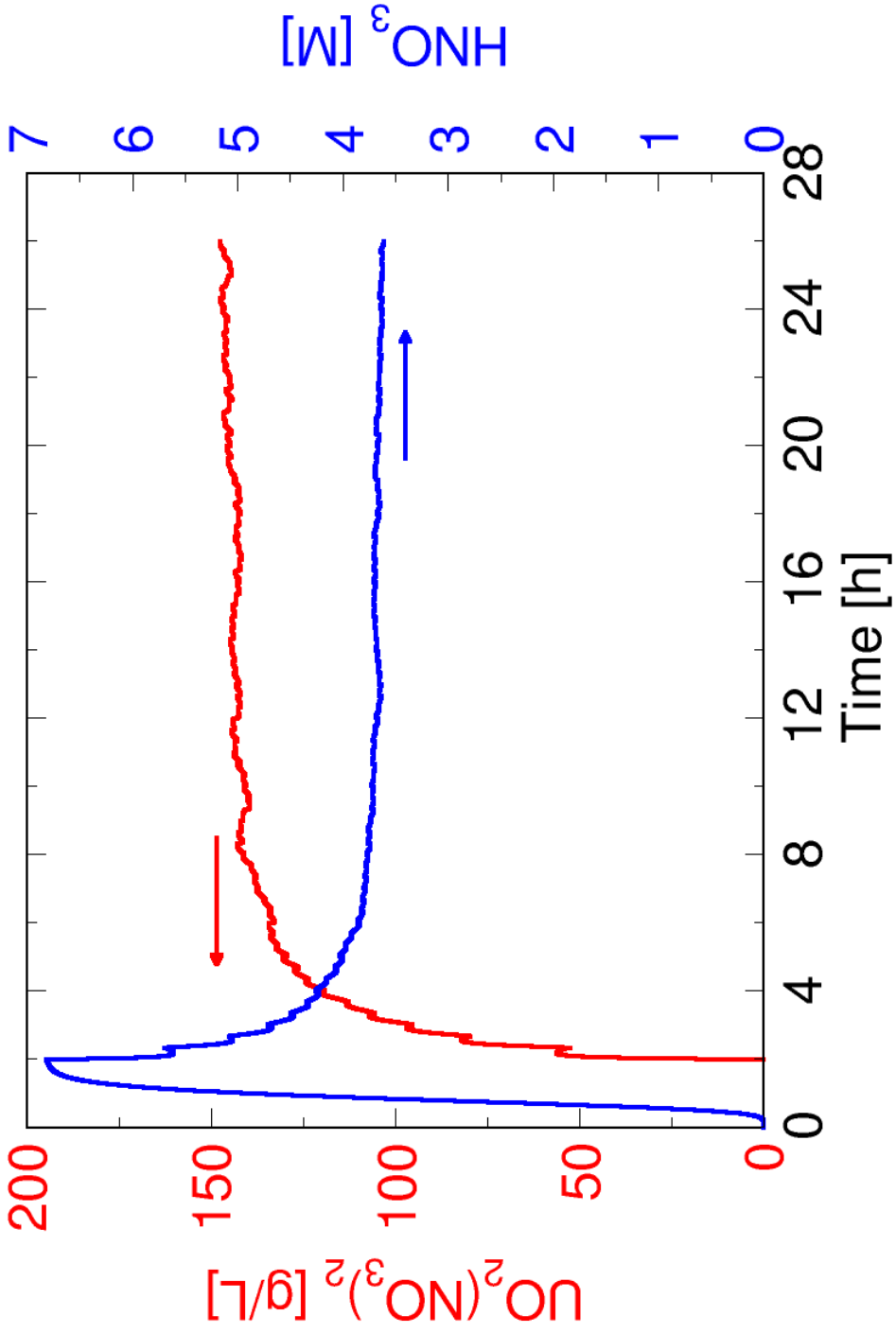

Fig. 6.3: ***Left ordinate axis:*** *Computed mass concentration of uranyl nitrate in the product stream.* ***Right ordinate axis:*** *Corresponding molarity of nitric acid. Capacity of* $0.5\,\mathrm{t\,d^{-1}}$.

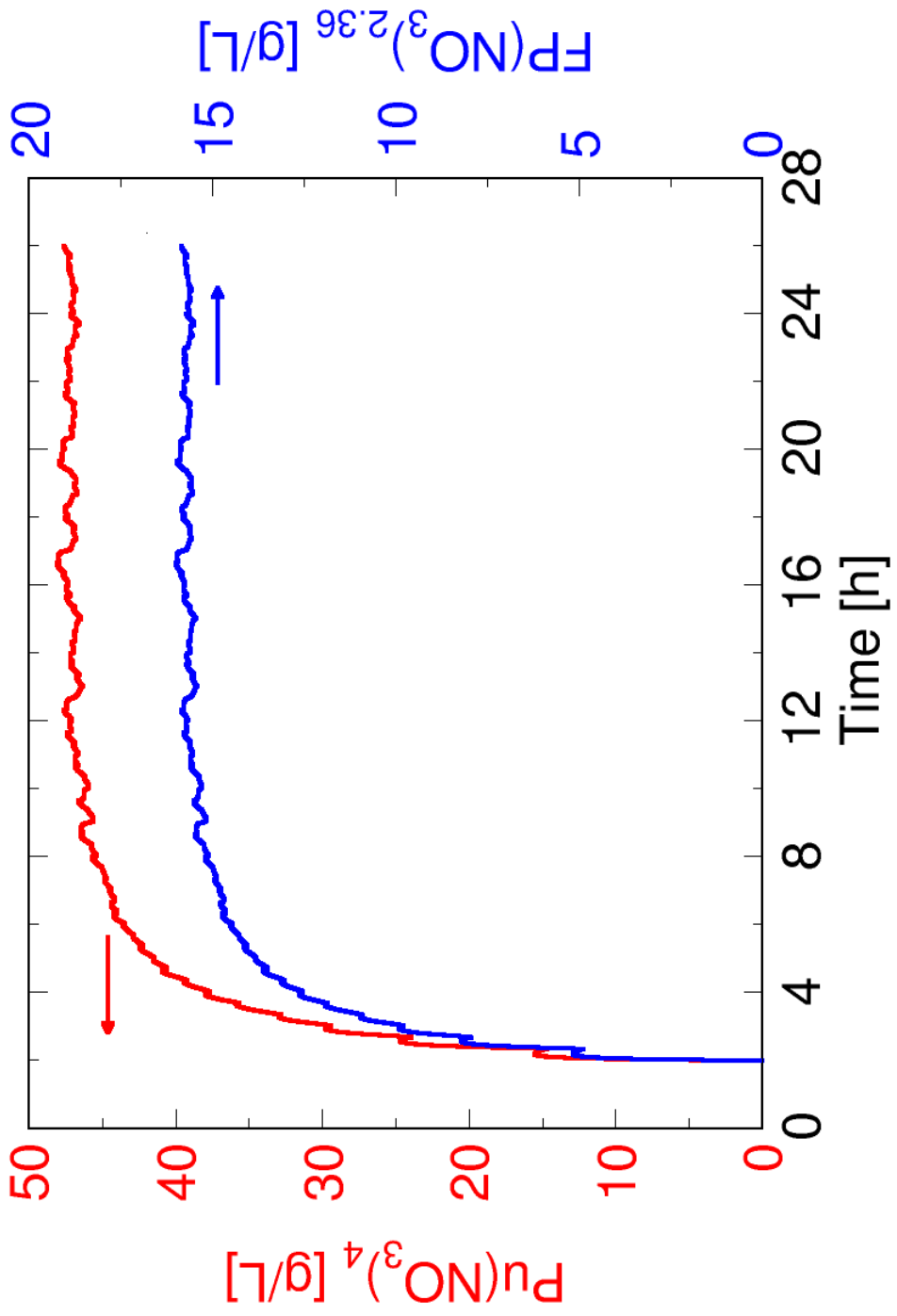

Fig. 6.4: ***Left ordinate axis:*** *Computed mass concentration of plutonium in the product stream.* ***Right ordinate axis:*** *Corresponding mass concentration of fission products. Capacity of* $0.5\,\mathrm{t\,d^{-1}}$.

6.1.2 Computed compartment results

Results in this section show quantities computed on a compartment basis.

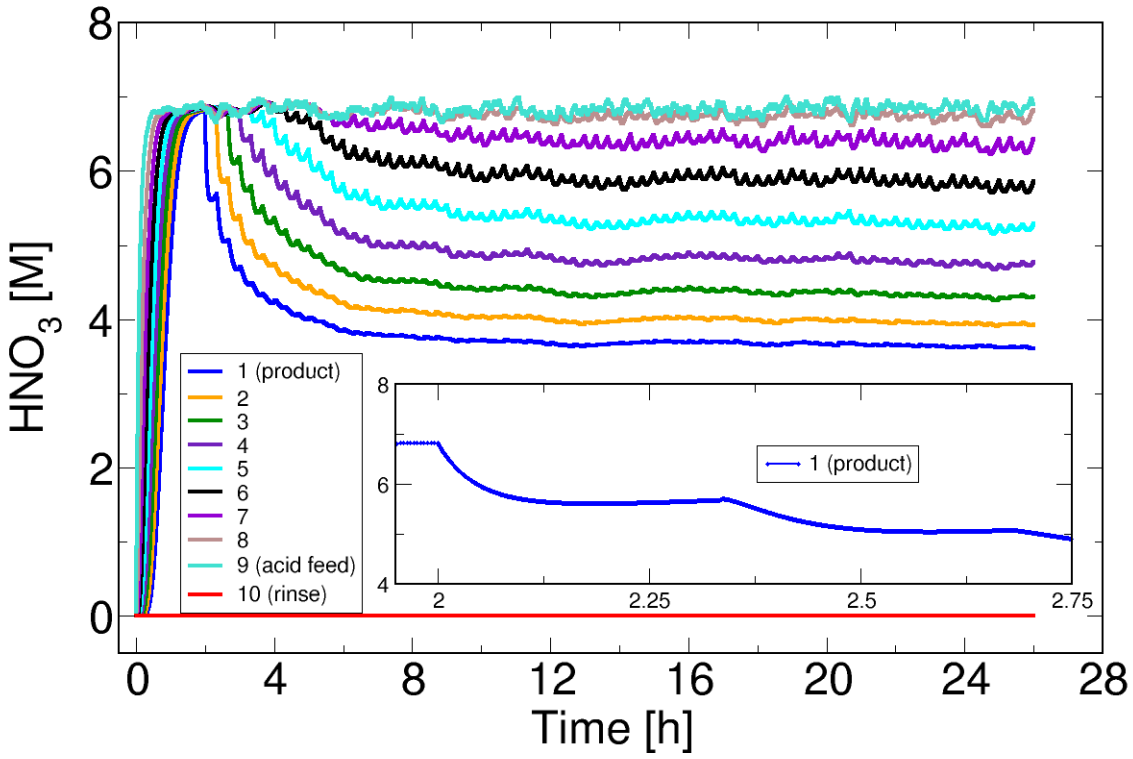

Fig. 6.5: *Nitric acid molarity for each compartment of the dissolver. Capacity of* $0.5\,\mathrm{t\,d^{-1}}$.

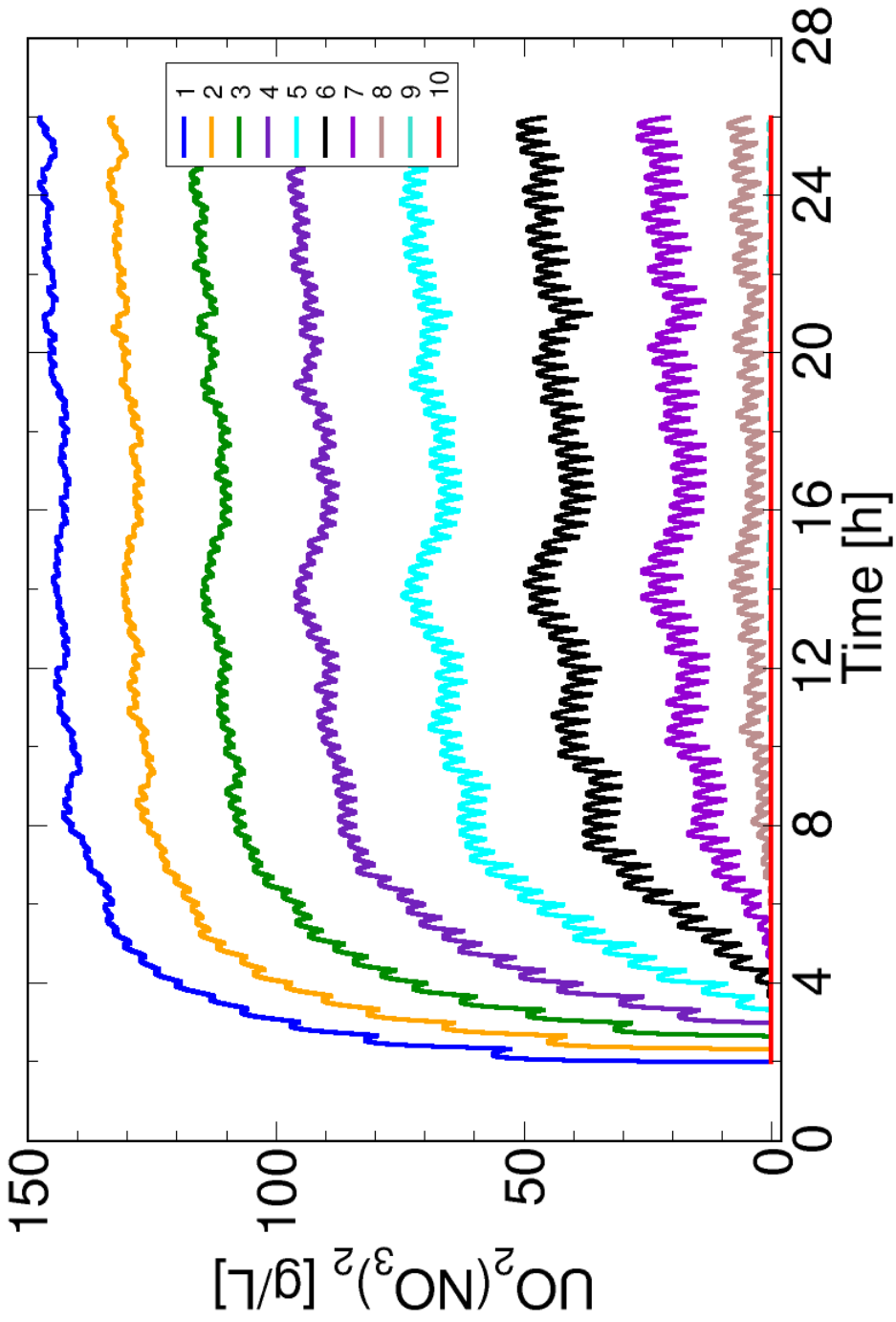

Fig. 6.6: *Uranyl nitrate mass concentration for each compartment of the dissolver. Capacity of* $0.5\,\mathrm{t\,d^{-1}}$.

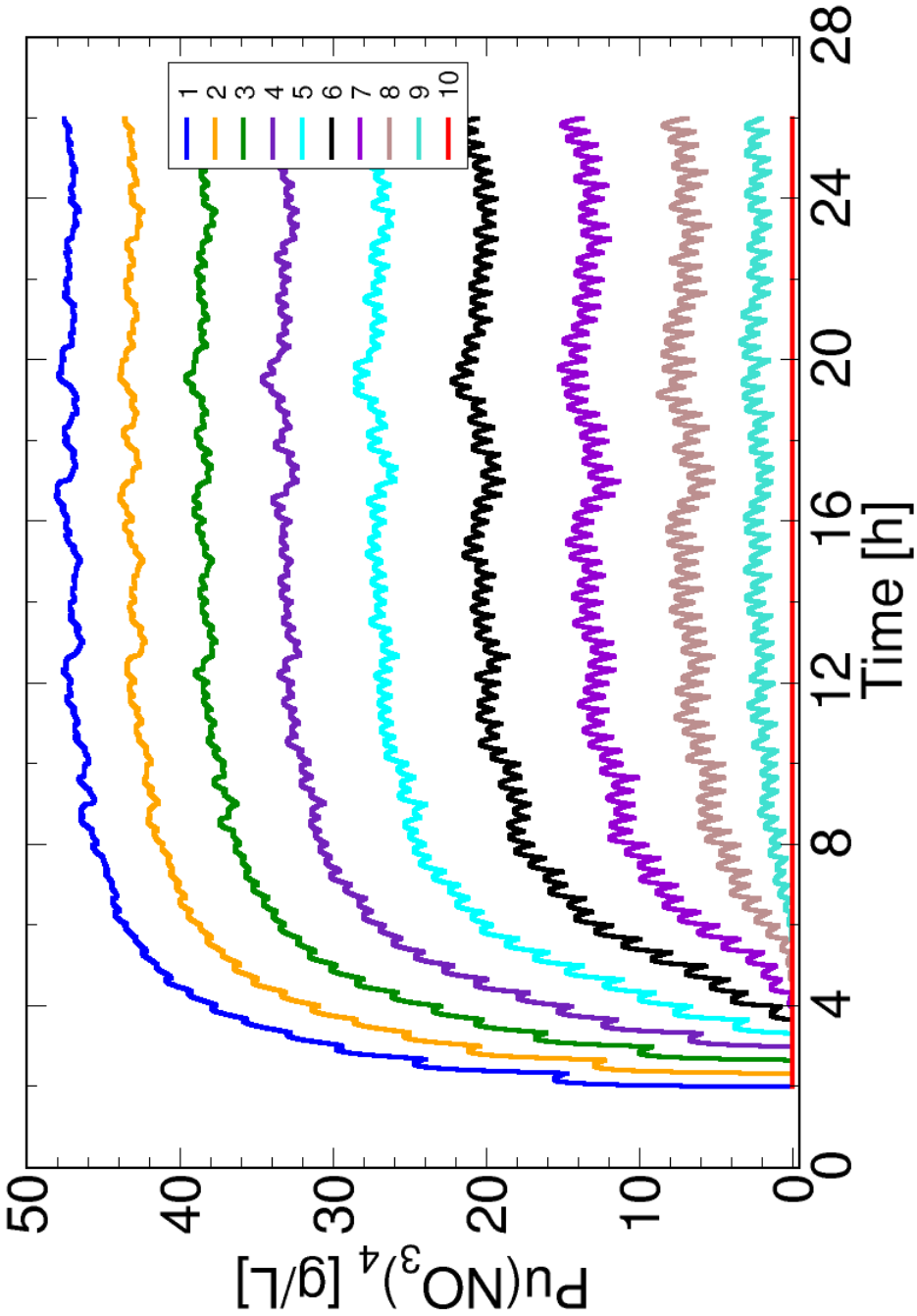

Fig. 6.7: *Plutonium nitrate mass concentration for each compartment of the dissolver. Capacity of* $0.5\,\mathrm{t\,d^{-1}}$.

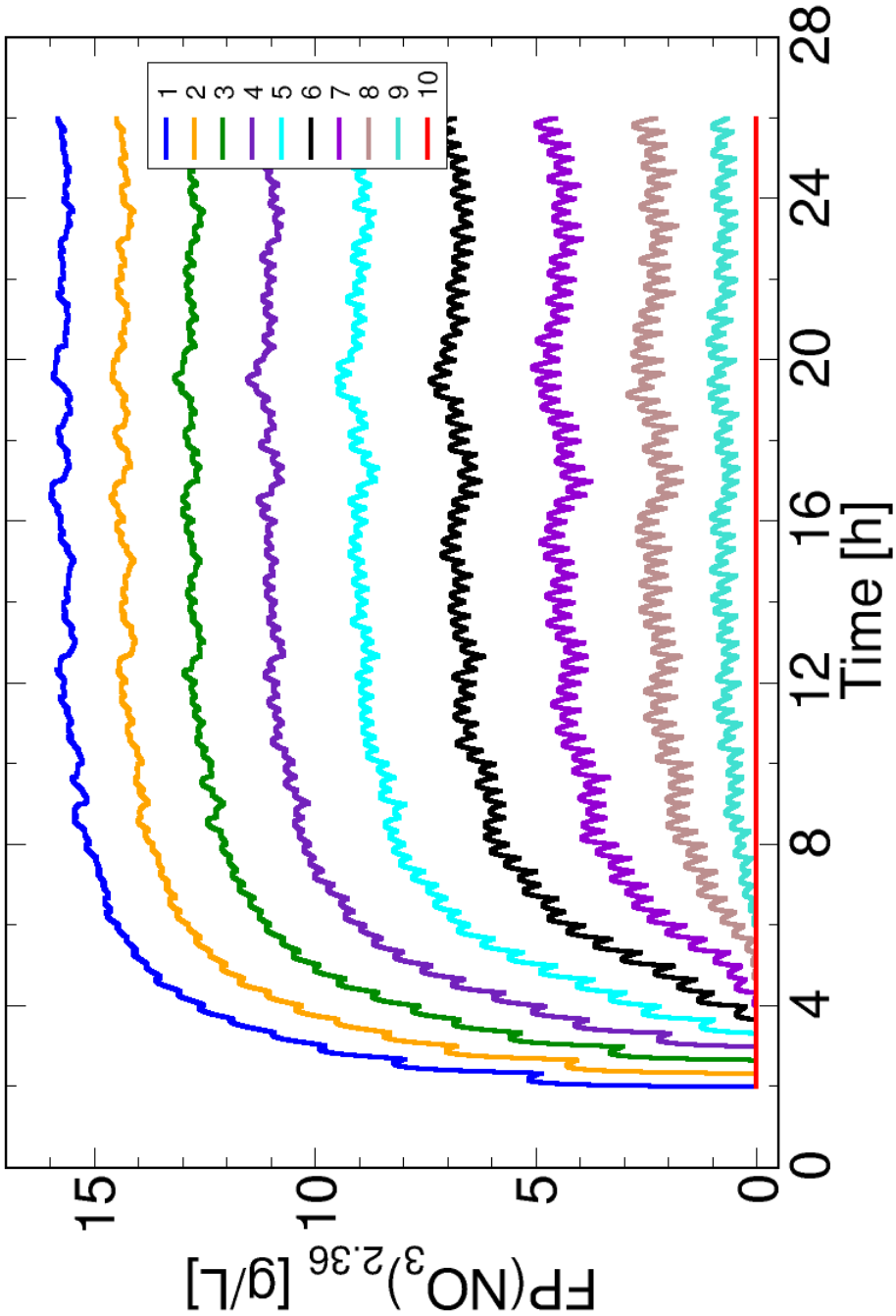

Fig. 6.8: *Fission products nitrate mass concentration for each compartment of the dissolver. Capacity of* $0.5\,\mathrm{t\,d^{-1}}$.

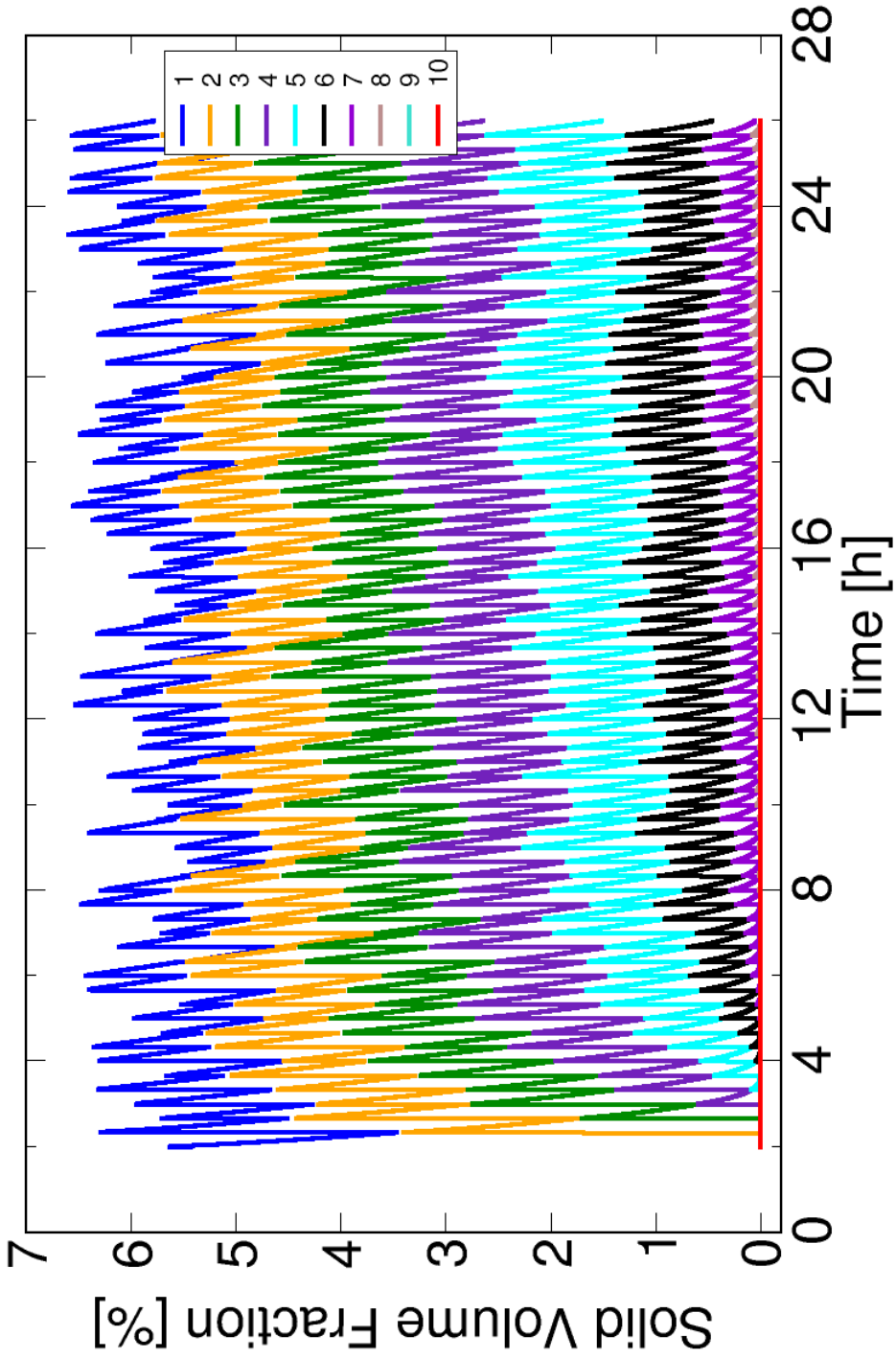

Fig. 6.9: *Solid volume fraction for each compartment of the dissolver. Capacity of* $0.5\,\mathrm{t\,d^{-1}}$.

6.2 Breeder reactor fuel at $1\,\mathrm{t\,d^{-1}}$ dissolution capacity

Results in this section utilize the same dissolver geometry (sec. A) as in the previous section but the operating parameters are modified to allow for a greater reprocessing capacity (tables 5.1 and 5.3).

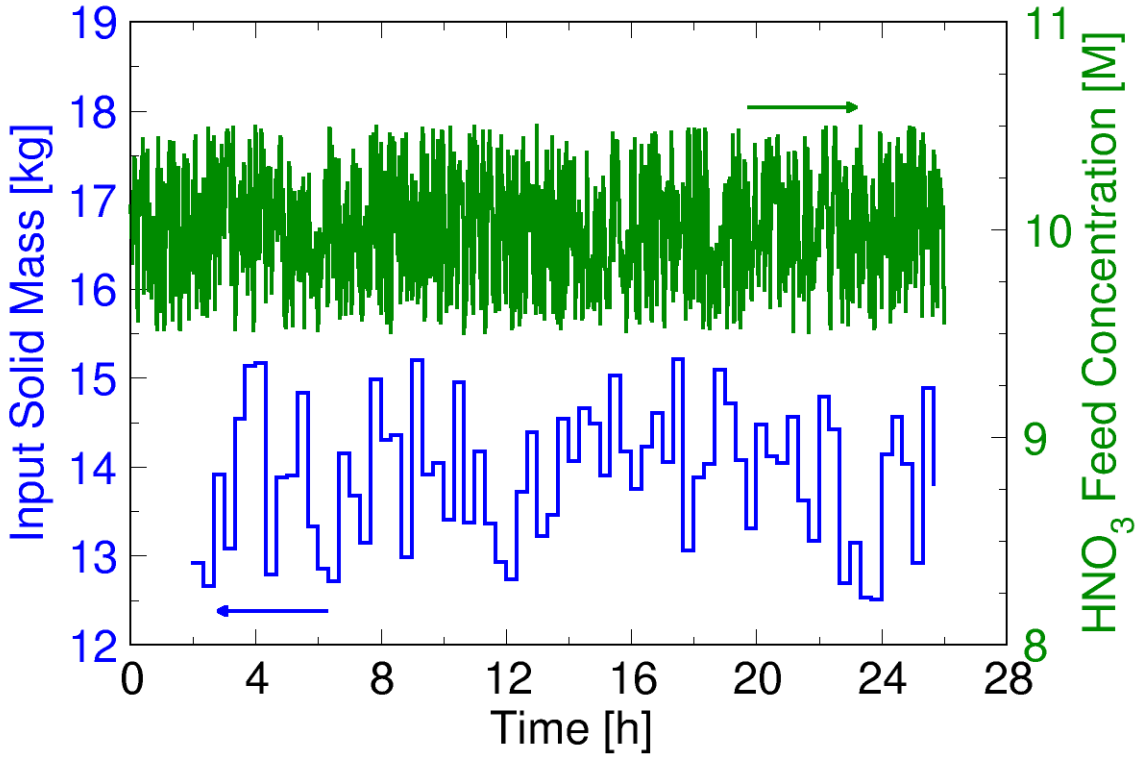

Fig. 6.10: ***Left ordinate axis:*** *Time variation of the mass of the solid loads in the first compartment inserted at each transfer period T_{trf}. This is a graphical representation of the piecewise constant, random function $\rho_s \mathscr{V}_s(t)$ created by imposing a random variation around the mean* $13.9\,\mathrm{kg}$. ***Right ordinate axis:*** *Input concentration of HNO_3 in the acid feed compartment ($k = 9$) with an imposed random variation around the mean* $10\,\mathrm{mol\,dm^{-3}}$. *This is the graphical representation of the piecewise linear random function $\mathscr{C}^{(9)}_{\mathrm{HNO_3}}(t)$.*

6.2.1 Computed product stream characteristics

The product stream exits the first compartment of the dissolver and it provides the primary data for coupling the dissolution with downstream processes such as digestors, holding tanks, etc. Therefore various plots representing the the time variation of the predicted results are presented in this section for the scaled up dissolution capacity of $1\,\mathrm{t\,d^{-1}}$.

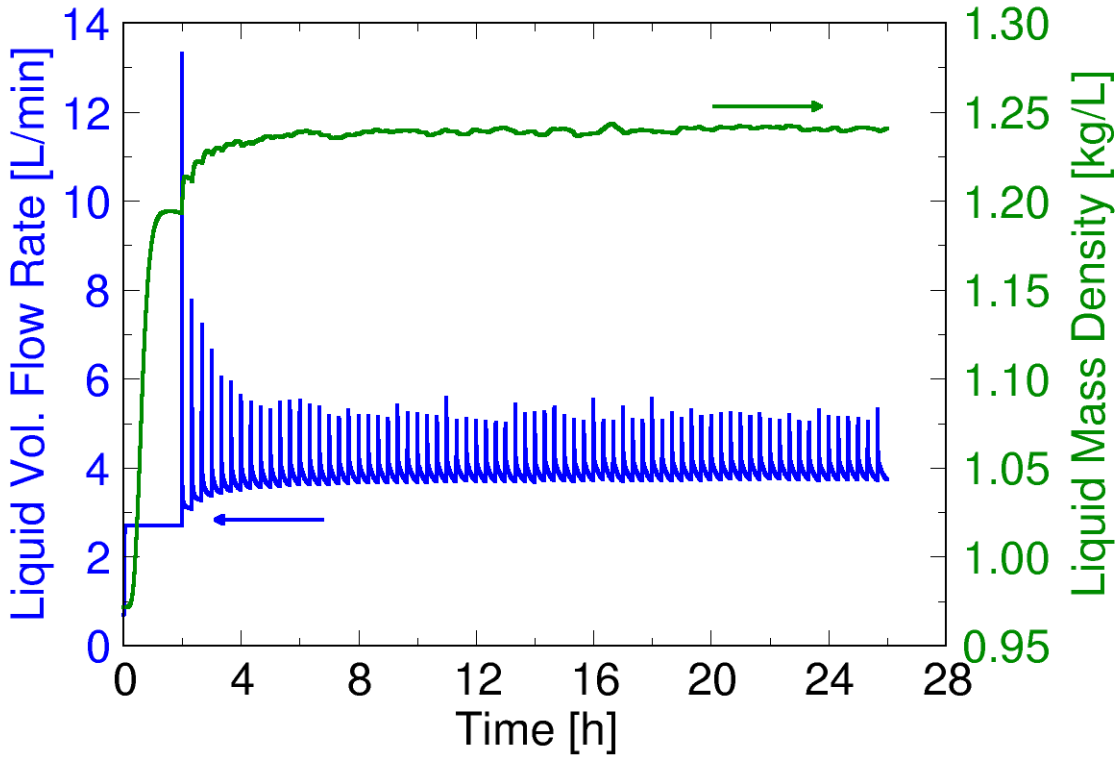

Fig. 6.11: ***Left ordinate axis:*** *Computed volumetric flow rate of the product stream.* ***Right ordinate axis:*** *Corresponding mass density. Capacity of* $1\,\mathrm{t\,d^{-1}}$.

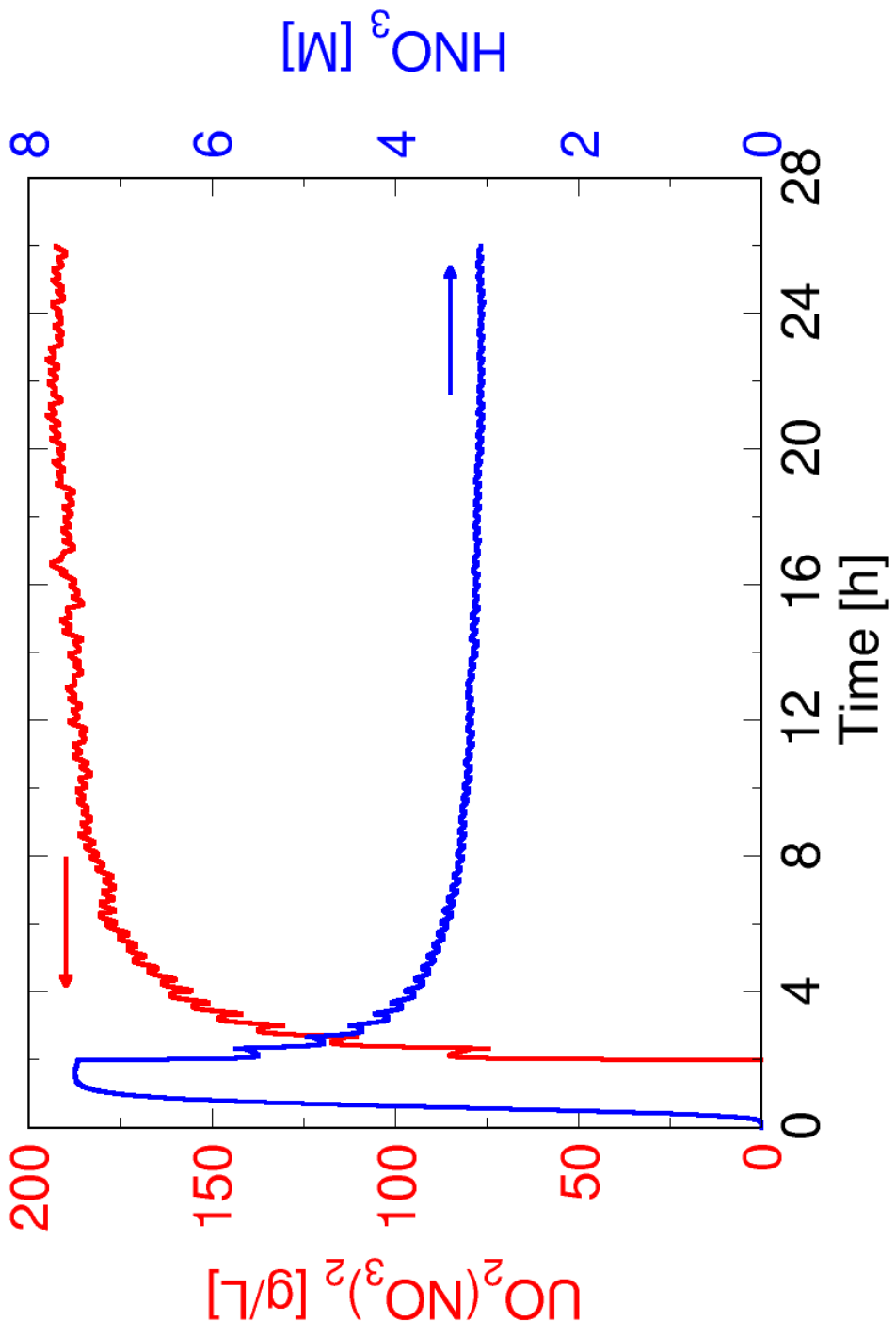

Fig. 6.12: ***Left ordinate axis:*** *Computed mass concentration of uranyl nitrate in the product stream.* ***Right ordinate axis:*** *Corresponding molarity of nitric acid. Capacity of* $1\,\mathrm{t\,d^{-1}}$.

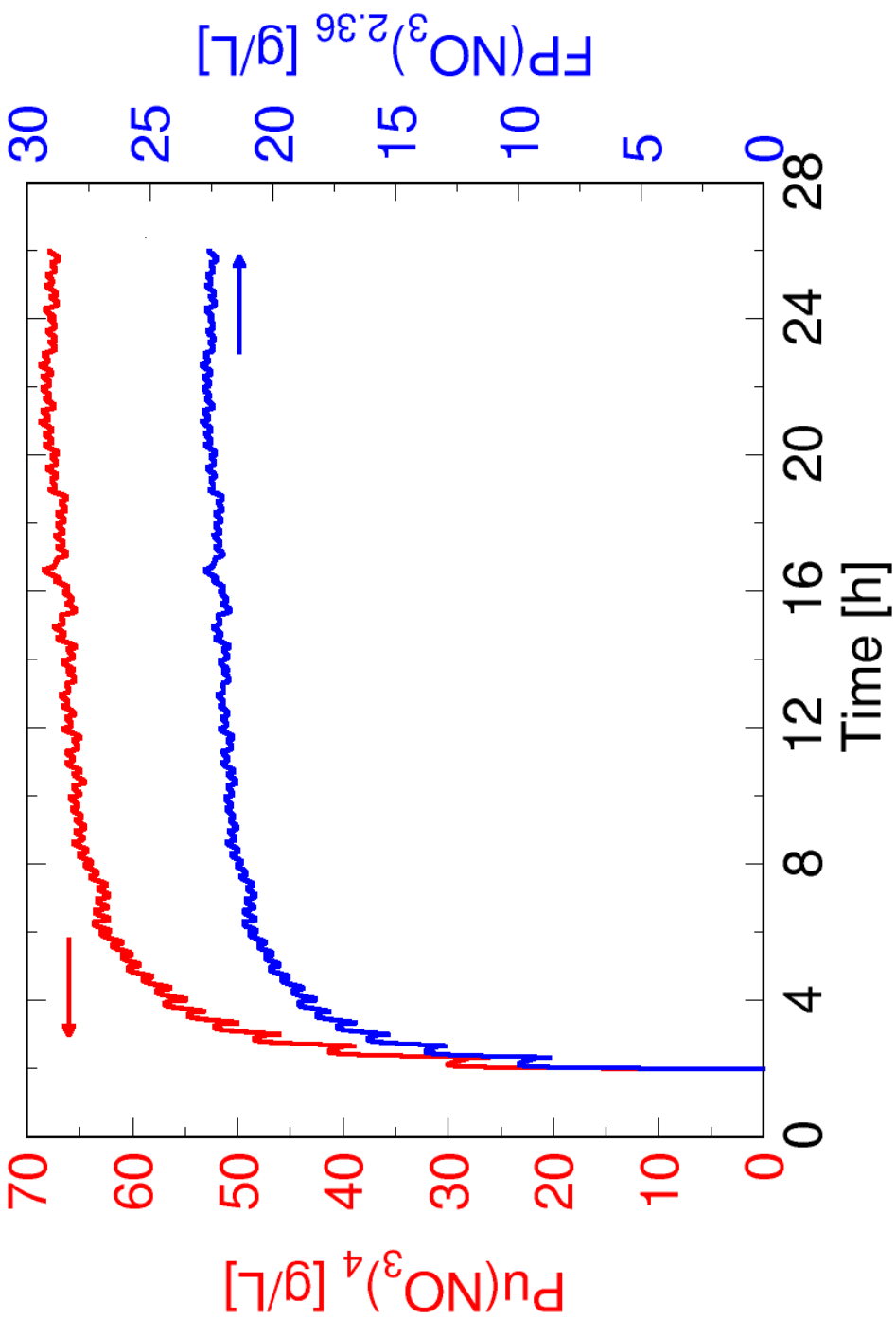

Fig. 6.13: ***Left ordinate axis:*** *Computed mass concentration of plutonium in the product stream.* ***Right ordinate axis:*** *Corresponding mass concentration of fission products. Capacity of* $1\,\mathrm{t\,d^{-1}}$.

6.2.2 Computed compartment results

Results in this section show quantities computed on a compartment basis.

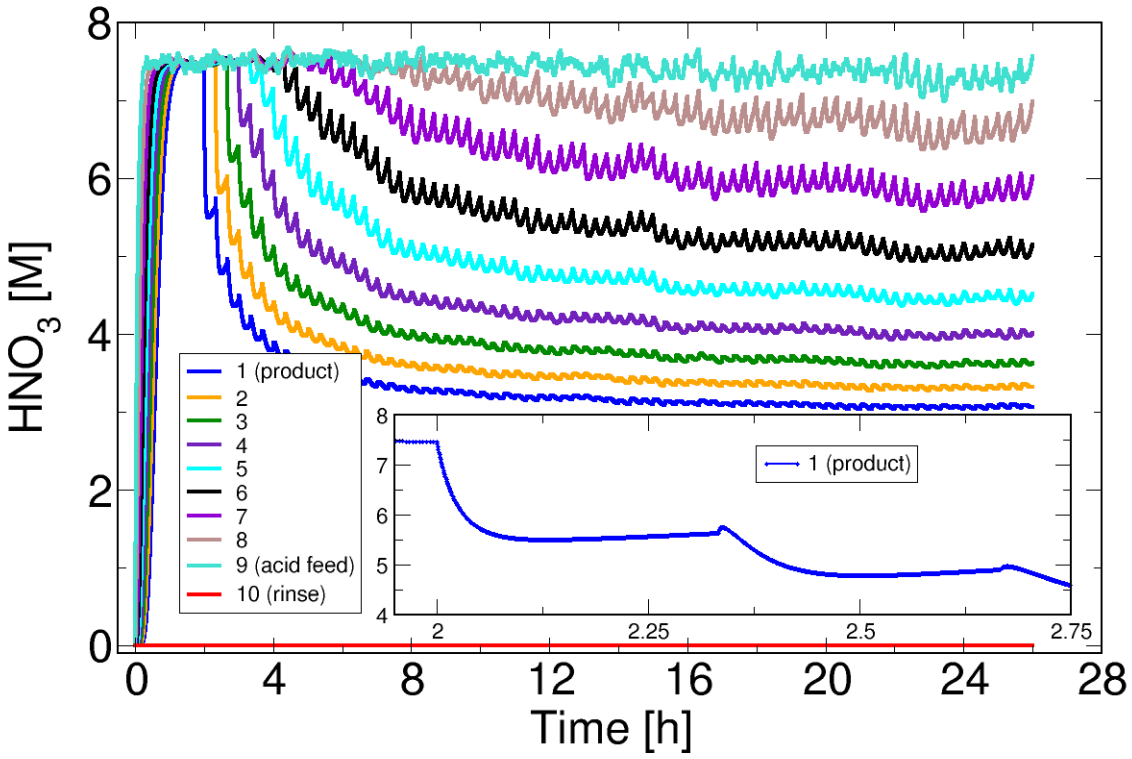

Fig. 6.14: *Nitric acid molarity for each compartment of the dissolver. Capacity of* $1\,\mathrm{t\,d^{-1}}$.

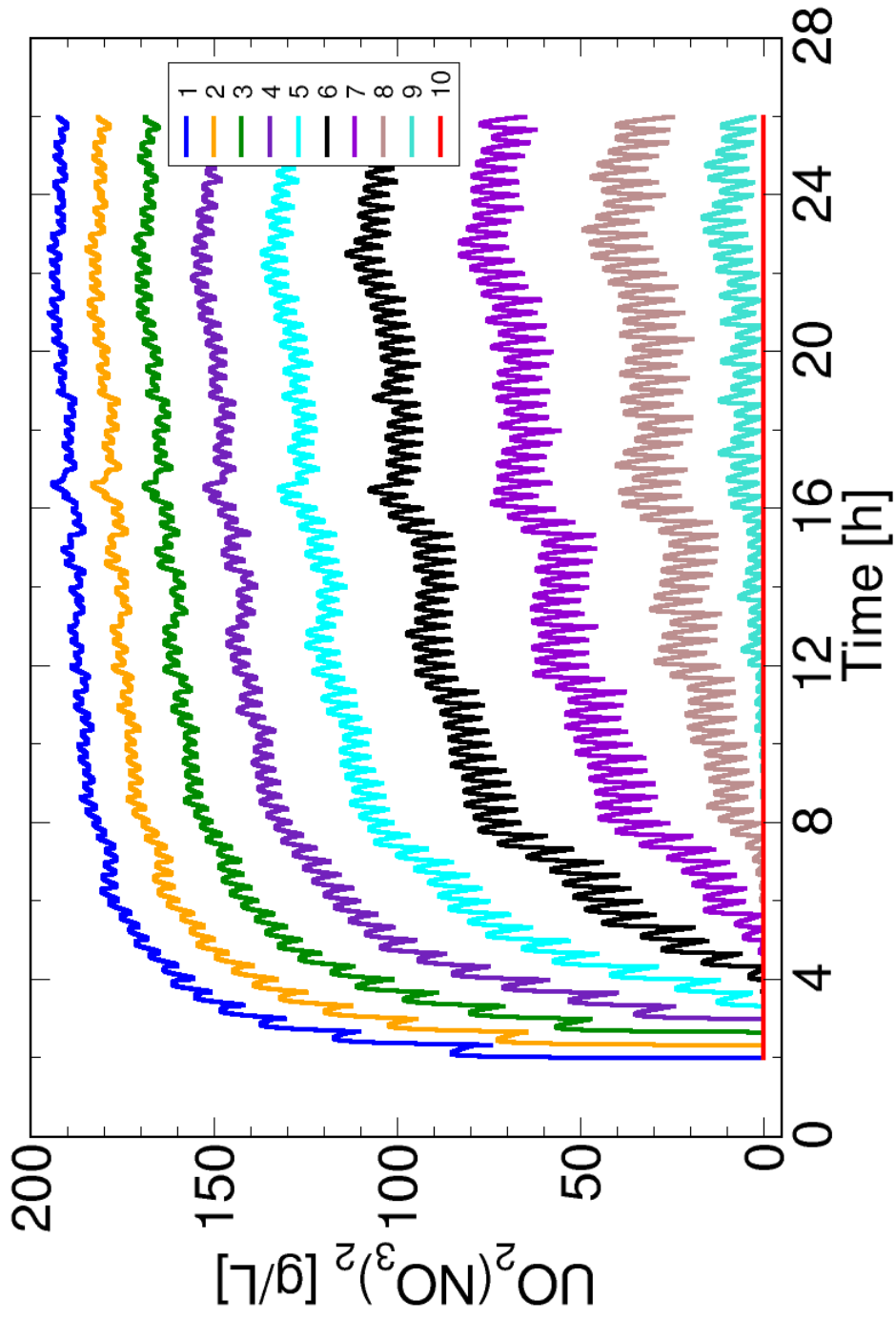

Fig. 6.15: *Uranyl nitrate mass concentration for each compartment of the dissolver. Capacity of* $1\,\mathrm{t\,d^{-1}}$.

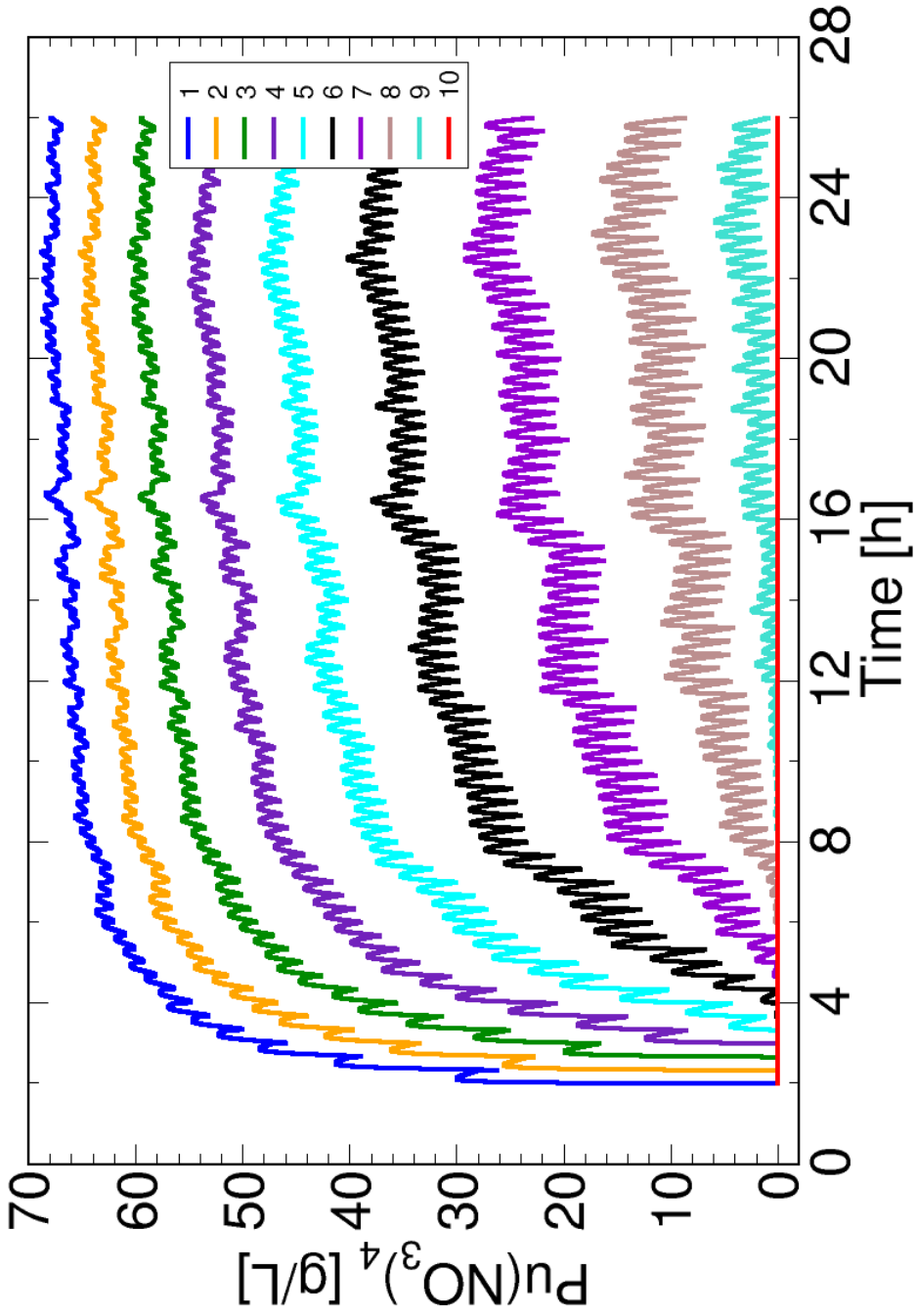

Fig. 6.16: *Plutonium nitrate mass concentration for each compartment of the dissolver. Capacity of* $1\,\mathrm{t\,d^{-1}}$.

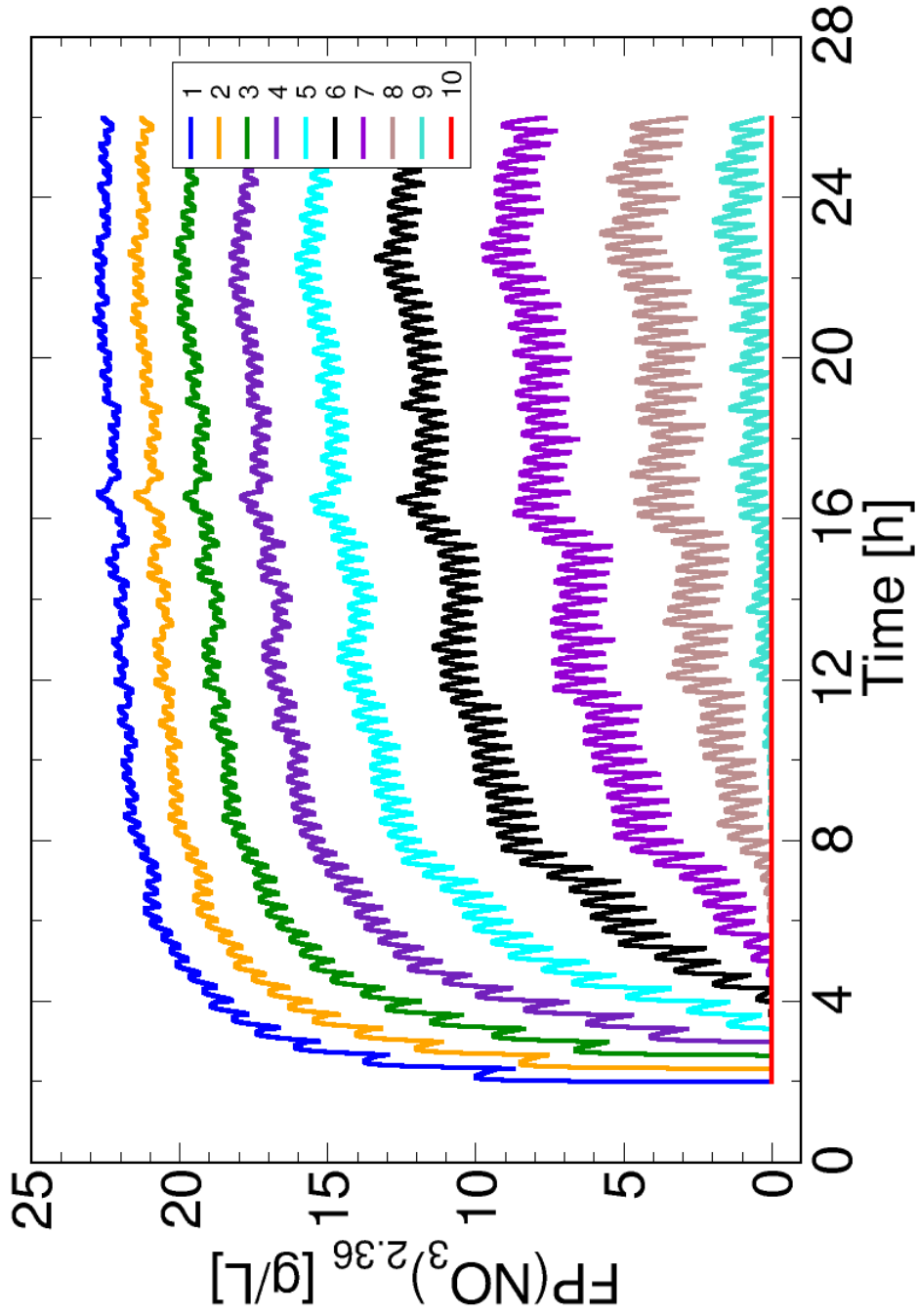

Fig. 6.17: *Fission products nitrate mass concentration for each compartment of the dissolver. Capacity of* $1\,\mathrm{t\,d^{-1}}$.

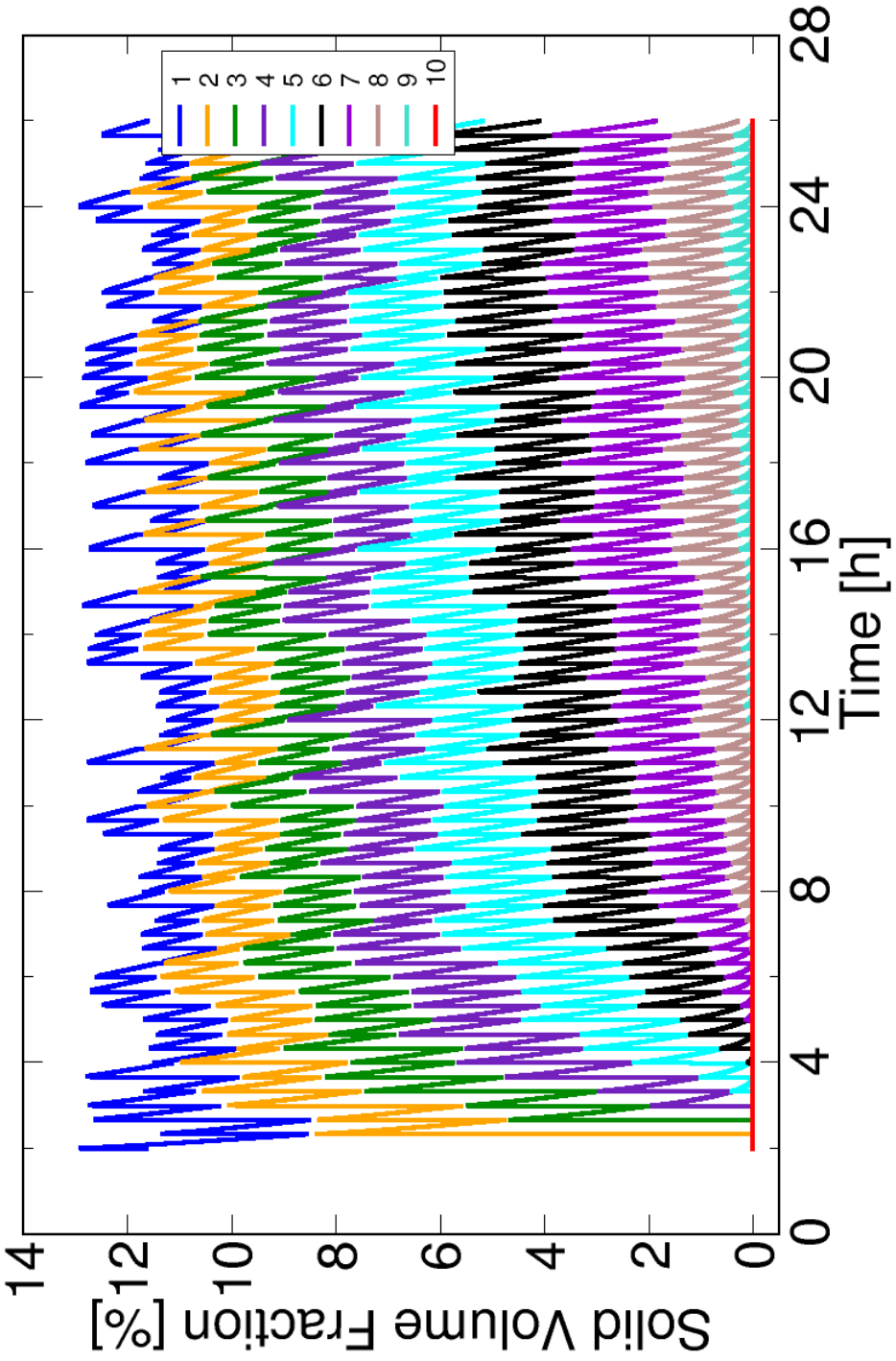

Fig. 6.18: *Solid volume fraction for each compartment of the dissolver. Capacity of* $1\,\mathrm{t\,d^{-1}}$.

6.3 LWR reactor fuel at $1.7\,\mathrm{t\,d^{-1}}$ dissolution capacity

In this test, a geometry scale-up is necessary. Here only a change in diameter of the rotary dissolver was attempted. In this case, the partition slots should be position such that a liquid depth corresponding to a 21 L-pool is available in each compartment of the dissolver (appendix A).

The results presented in this section were used to test the computer program provided to the Separations and Safeguards Peformance Model (SSPM) code (Cipiti and McDaniel, 2011; Cipiti et al., 2009). The program was written in MATLAB language as a stand-alone module that can be invoked by the Simulink environment used in the SSPM application. There are still significant challenges to integrate modules into existing plant-level computational environments. The present application is an example of a model that may require continuous variation of inputs therefore making it difficult to couple, mathematically, with exterior models. The work done here follows a commonality design approach (de Almeida, 2011) to enable mathematical coupling. Work in progress for testing the coupling method with the SSPM is described by Cipiti and McDaniel (2011). Future work will focus in evaluating proper time evolution of the coupled systems.

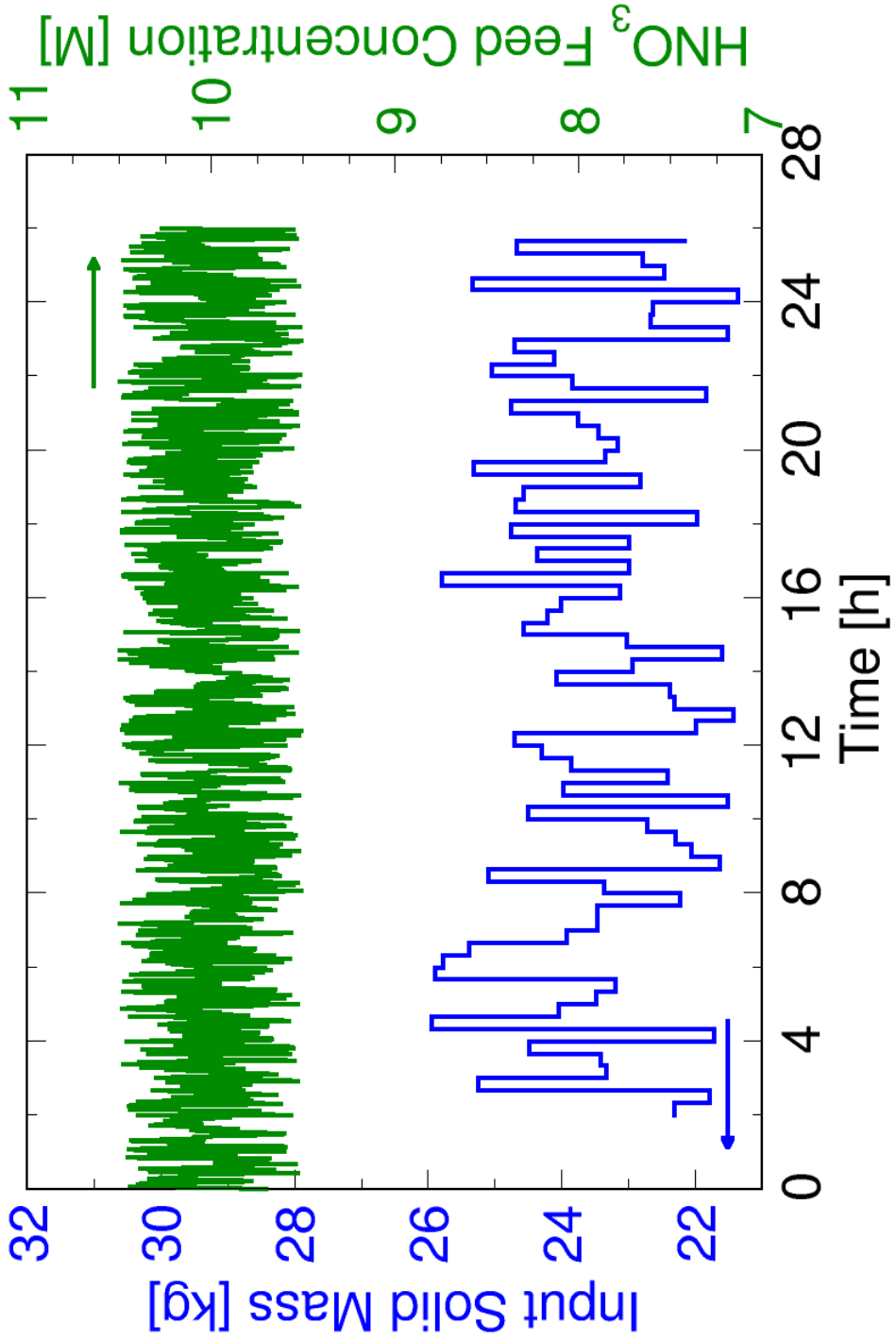

Fig. 6.19: ***Left ordinate axis:*** *Time variation of the mass of the solid loads in the first compartment inserted at each transfer period T_{trf}. This is a graphical representation of the piecewise constant, random function $\rho_s \mathscr{Y}_s(t)$ created by imposing a random variation around the mean* 23.6 kg. ***Right ordinate axis:*** *Input concentration of HNO_3 in the acid feed compartment ($k = 9$) with an imposed random variation around the mean* $10\,\mathrm{mol\,dm^{-3}}$. *This is the graphical representation of the piecewise linear random function $\mathscr{C}^{(9)}_{\mathrm{HNO_3}}(t)$.*

6.3.1 Computed product stream characteristics

Here the primary output data provided to the SSPM application are shown in graphic form.

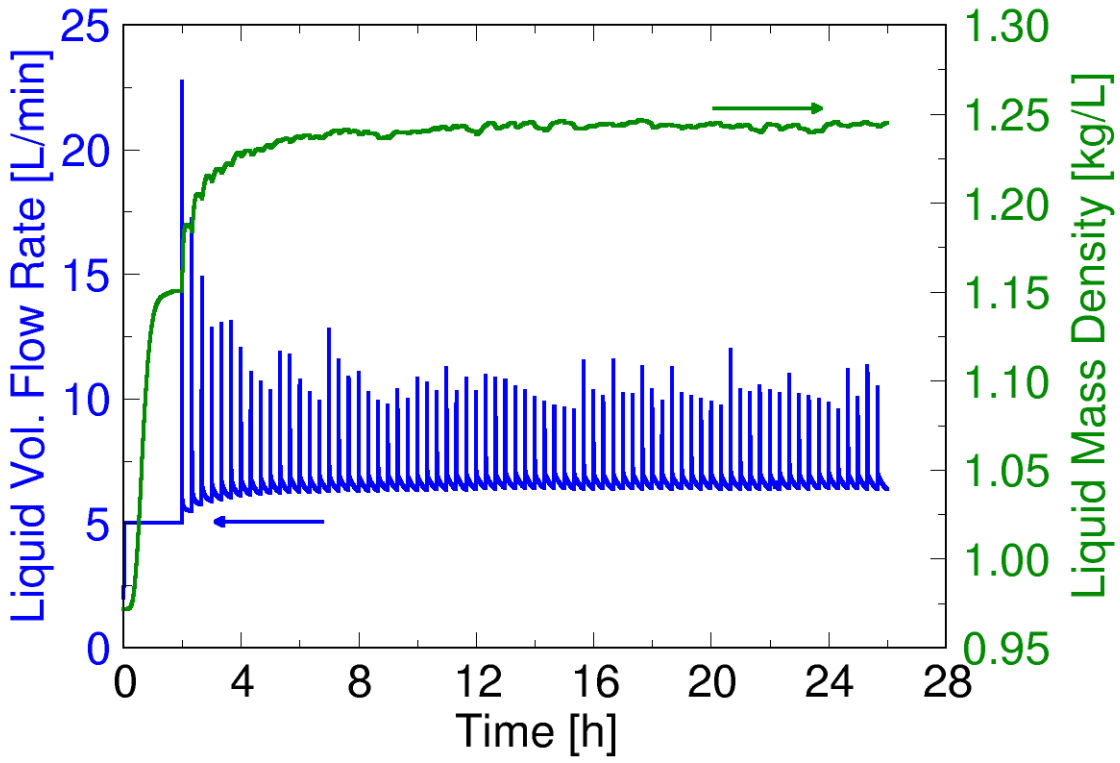

Fig. 6.20: ***Left ordinate axis:*** *Computed volumetric flow rate of the product stream.* ***Right ordinate axis:*** *Corresponding mass density. Capacity of* $1.7\,\mathrm{t\,d^{-1}}$.

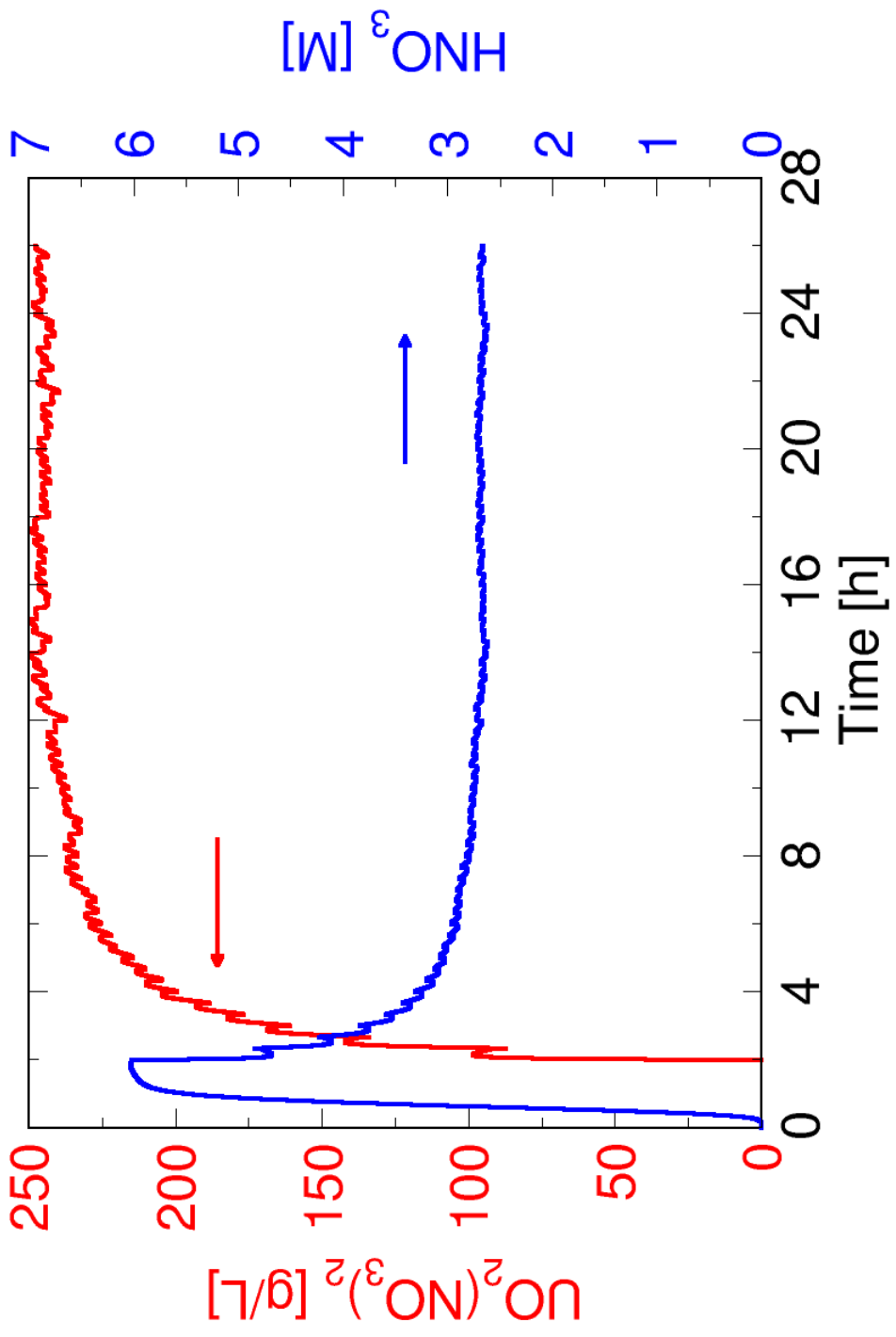

Fig. 6.21: ***Left ordinate axis:*** *Computed mass concentration of uranyl nitrate in the product stream.* ***Right ordinate axis:*** *Corresponding molarity of nitric acid. Capacity of* $1.7\,\mathrm{t\,d^{-1}}$.

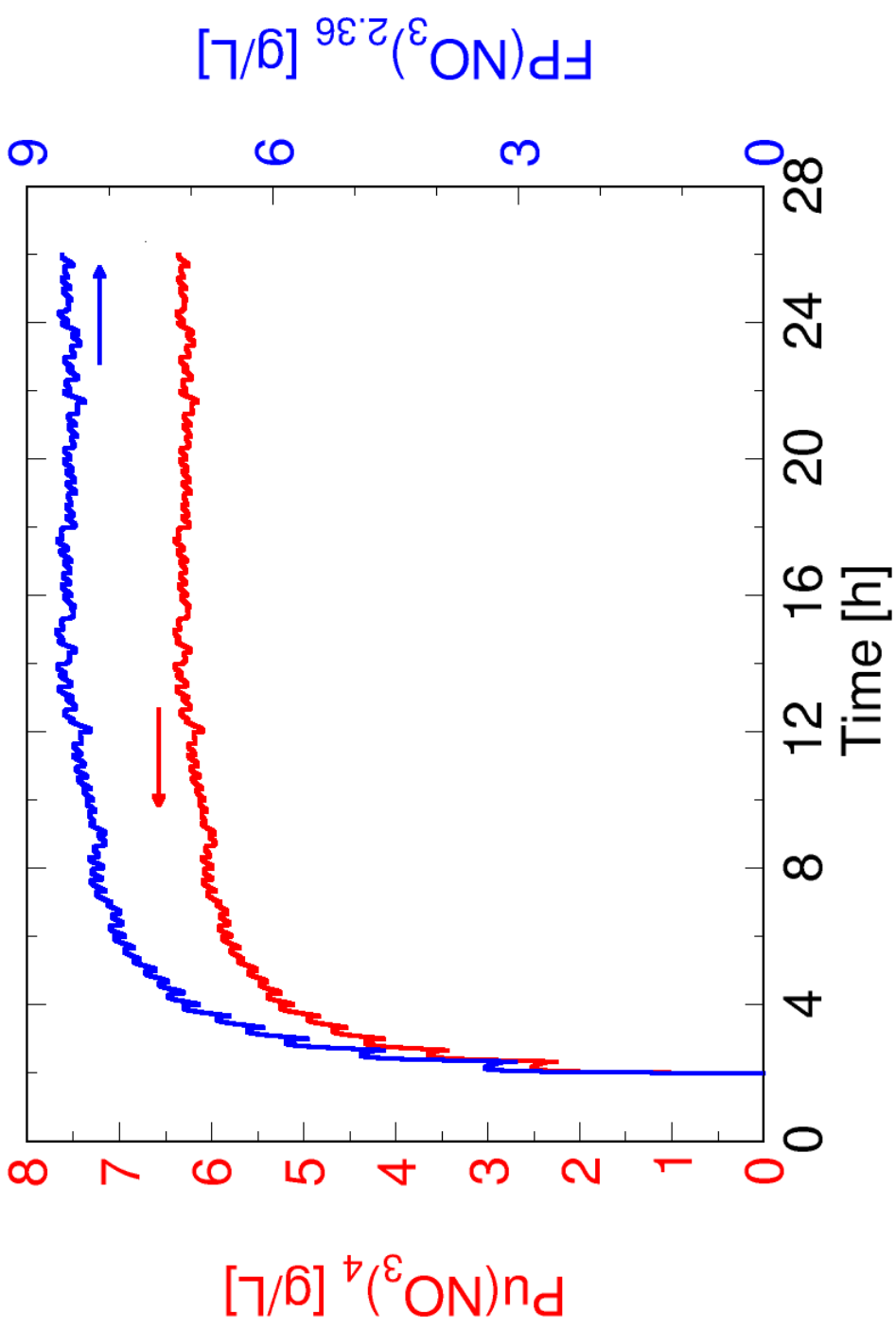

Fig. 6.22: ***Left ordinate axis:*** *Computed mass concentration of plutonium in the product stream.* ***Right ordinate axis:*** *Corresponding mass concentration of fission products. Capacity of* $1.7\,\mathrm{t\,d^{-1}}$.

6.3.2 Computed compartment results

Results in this section show quantities computed on a compartment basis.

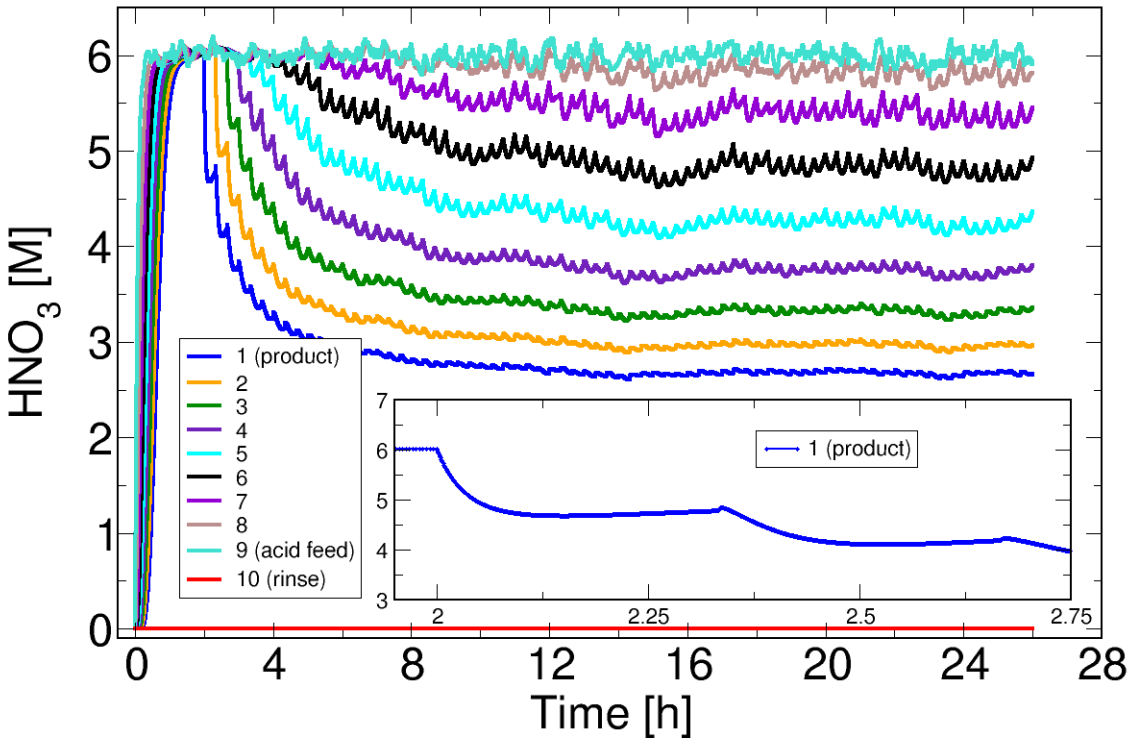

Fig. 6.23: *Nitric acid molarity for each compartment of the dissolver. Capacity of* $1.7\,\mathrm{t\,d^{-1}}$.

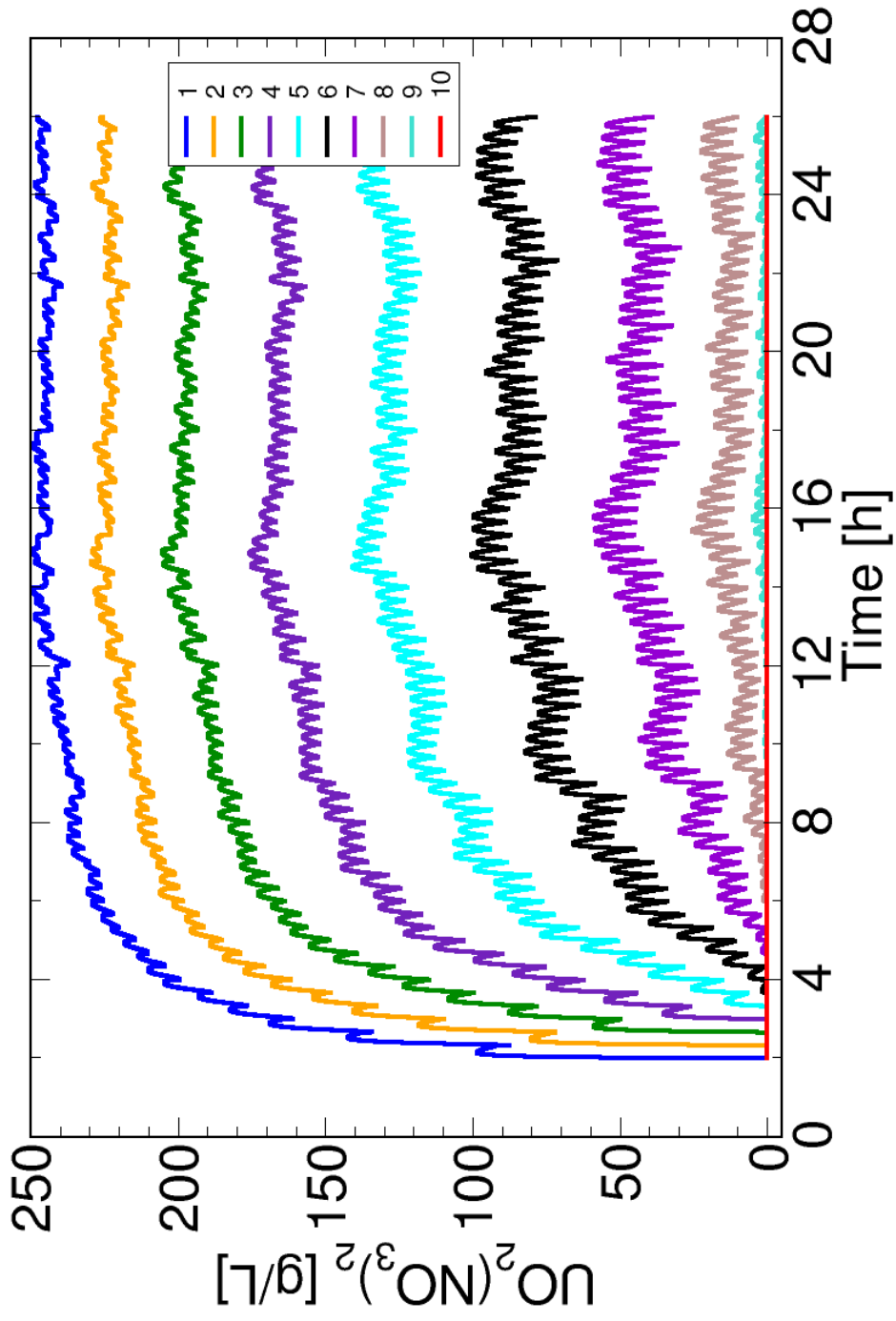

Fig. 6.24: *Uranyl nitrate mass concentration for each compartment of the dissolver. Capacity of* $1.7\,\mathrm{t\,d^{-1}}$.

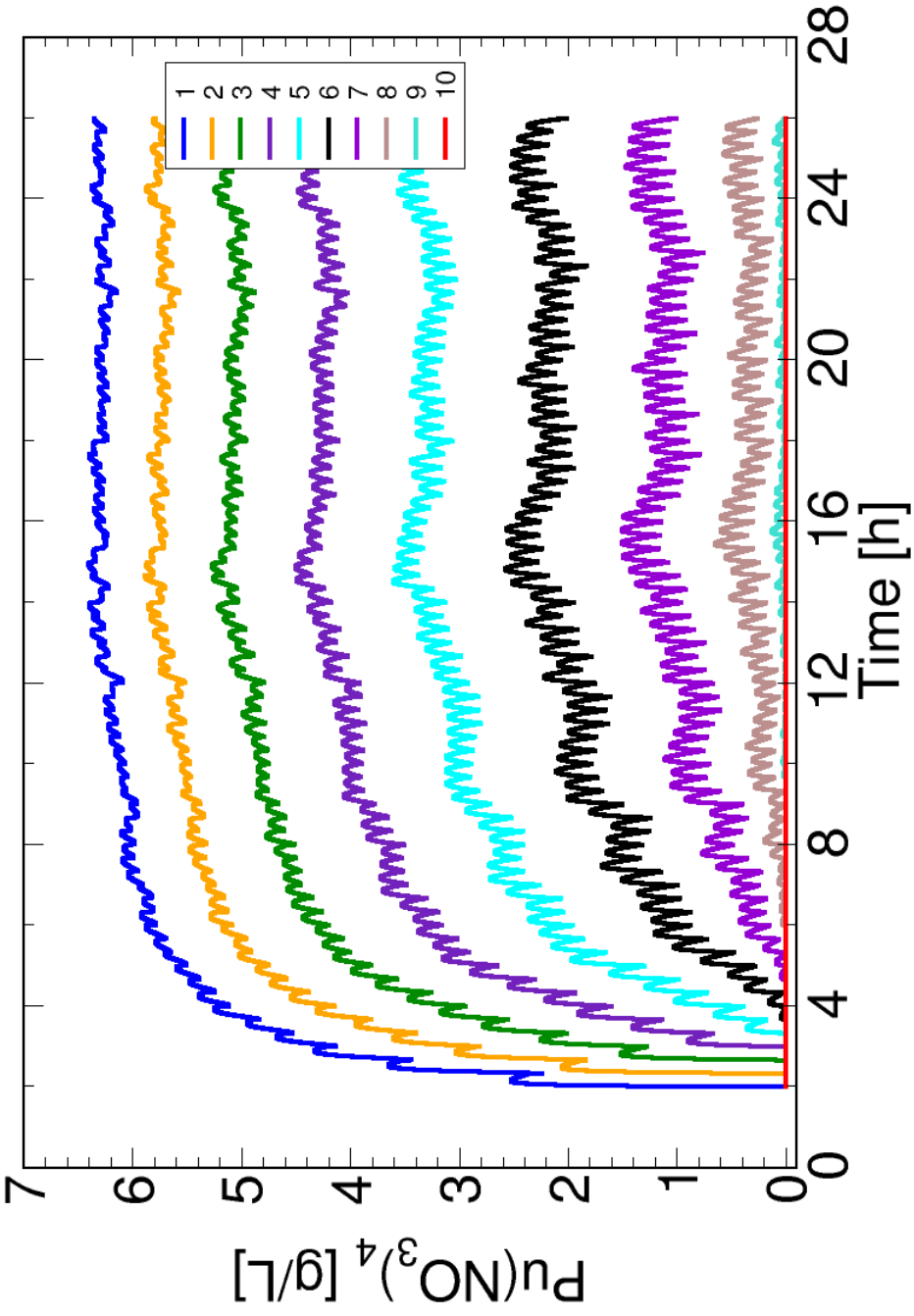

Fig. 6.25: *Plutonium nitrate mass concentration for each compartment of the dissolver. Capacity of* $1.7\,\mathrm{t\,d^{-1}}$.

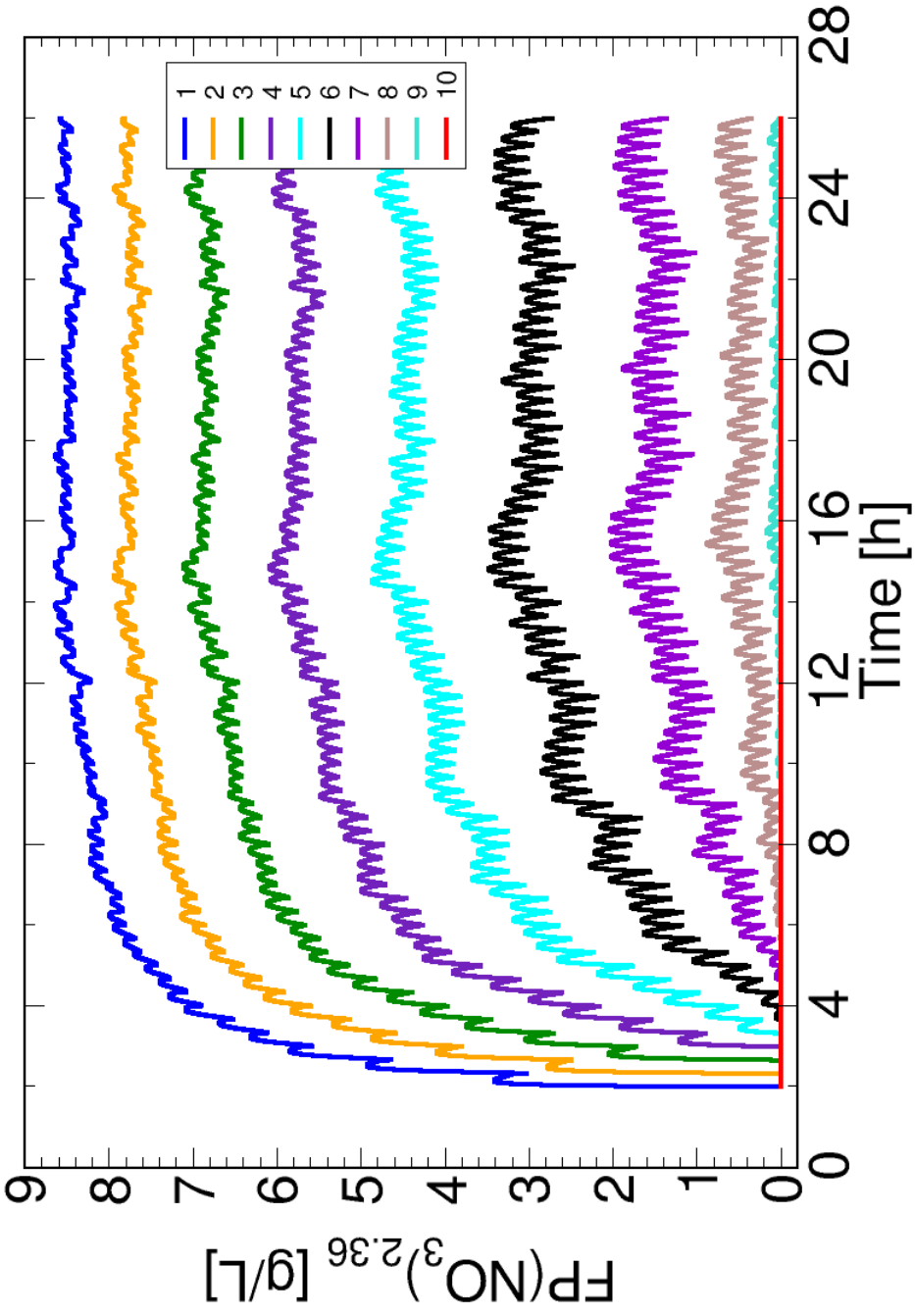

Fig. 6.26: *Fission products nitrate mass concentration for each compartment of the dissolver. Capacity of* $1.7\,\mathrm{t\,d^{-1}}$.

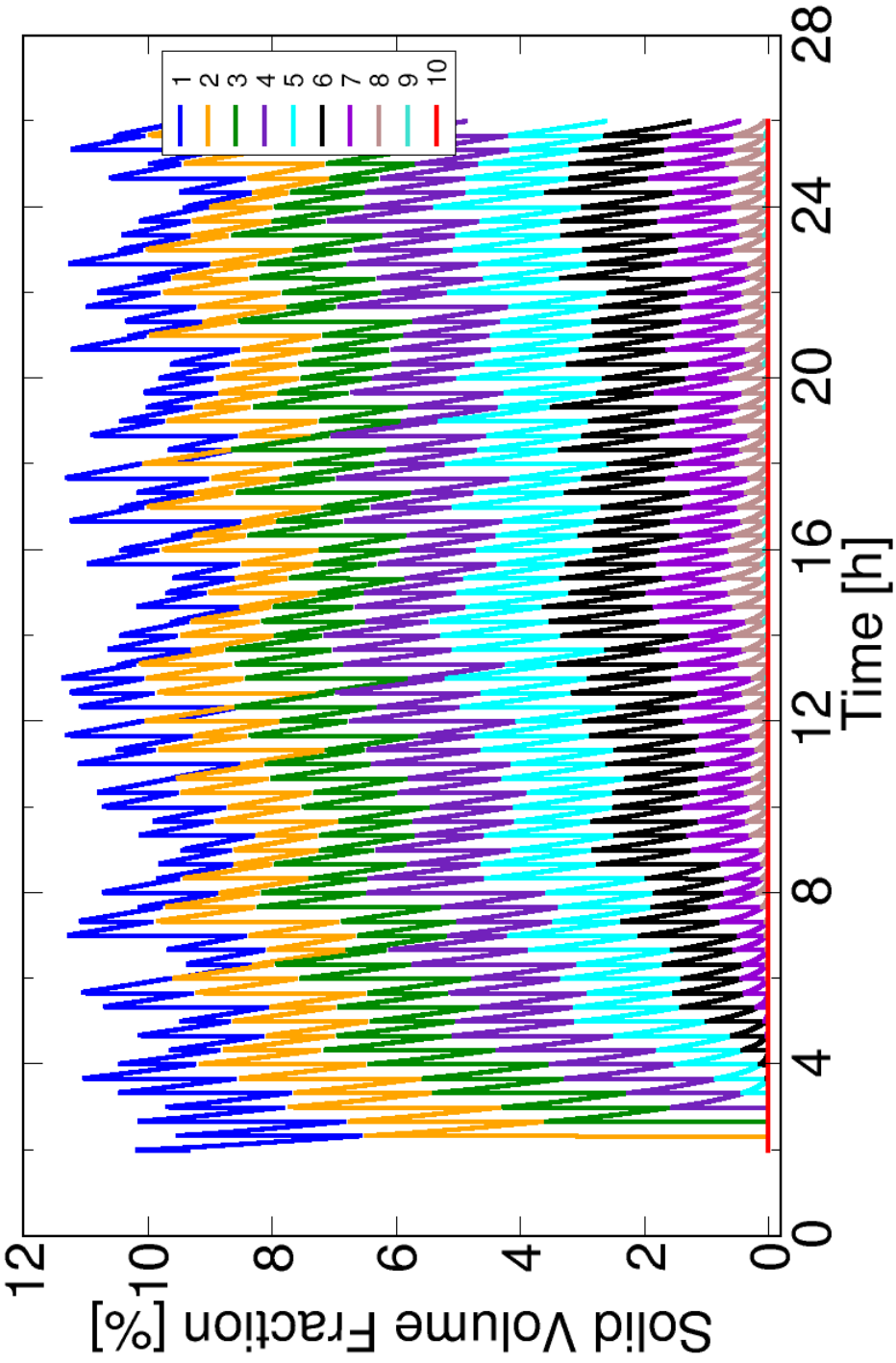

Fig. 6.27: *Solid volume fraction for each compartment of the dissolver. Capacity of* $1.7\,\mathrm{t\,d^{-1}}$.

7 Verification method

A program for rigorous verification of the prototyped computer code developed for obtaining the results presented (sec. 6) has not been advanced at this point. However, the mathematical description of problem (4.23)–(4.25) allows for the development of a systematic method of manufactured solutions to be used to verify the order of convergence of the numerical method (Knupp and Salari, 2007). In addition, in view of the usage of the DAE solver DASPK, sensitivity analysis is readily available to support verification of the solution method. These efforts need to be carried out in the future and results reported in a corresponding communication.

8 Uncertainty

A validation test was made against available but limited experimental data. The results obtained compared very well against the experimental data and against a previous model described in Lewis and Weber (1980).

In this experimental procedure for model validation, only the liquid phase is involved. A water feed stream enters the discharge compartment of a rotary dissolver with time variations representative of a device startup, processing, and shutdown operations (fig. 8.1). Simultaneously, the variation of the nitric acid in the feed stream to the discharge compartment follows the curve in figure 8.2. The problem (4.23)–(4.25) was modified to the extent possible to closely match the model in Lewis and Weber (1980). The network model (sec. 3) was also reduced to nine compartments. With these modifications, and using parameters from Lewis and Weber (1980), a solution to the concentration of nitric acid in the network was obtained and the result for the first compartment compared with experimental measurements; the comparison is within 3 % agreement (fig. 8.3).

This preliminary validation exercise helped obtain confidence on the model development and its implementation. However it lacks much of the important aspects of the system's operation, in particular no solids and no dissolution are present. If they were, access to experimental data would be very difficult if at all possible. A plan for validation and uncertainty quantification is within the objective of future efforts. Such plan is achievable when a rigorous mathematical foundation is at hand.

9 Fidelity improvement

It was briefly mentioned in section 4.2.1 that difficulties in measuring a dissolving surface area can lead to great errors in predictions of dissolution rates. Therefore improvements on how to better estimate the roughness factor and/or compute the

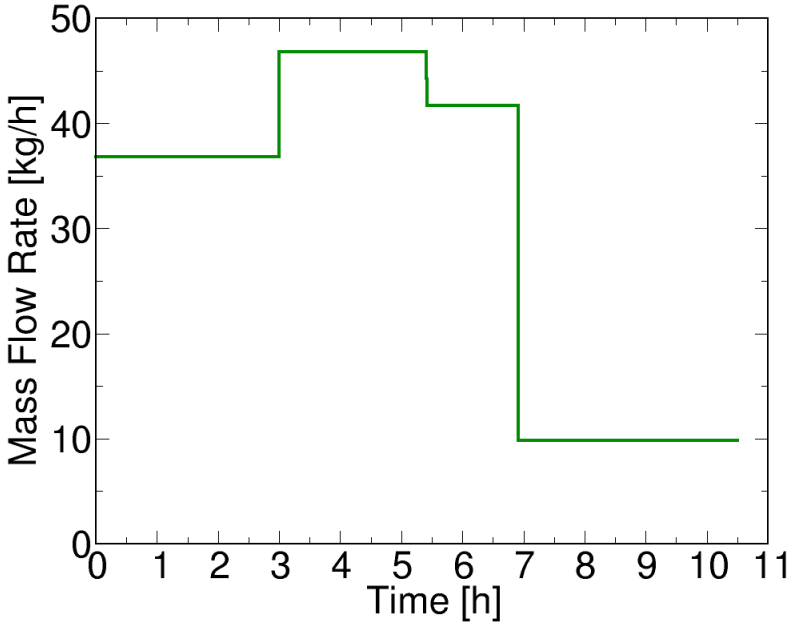

Fig. 8.1: *Liquid mass flow rate feed variation in the discharge compartment for model validation.*

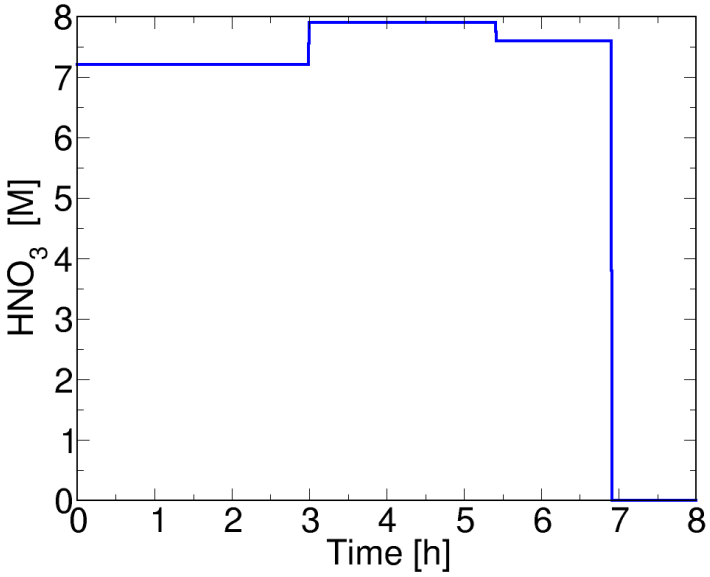

Fig. 8.2: *Nitric acid molarity variation in the feed stream in the discharge compartment for model validation.*

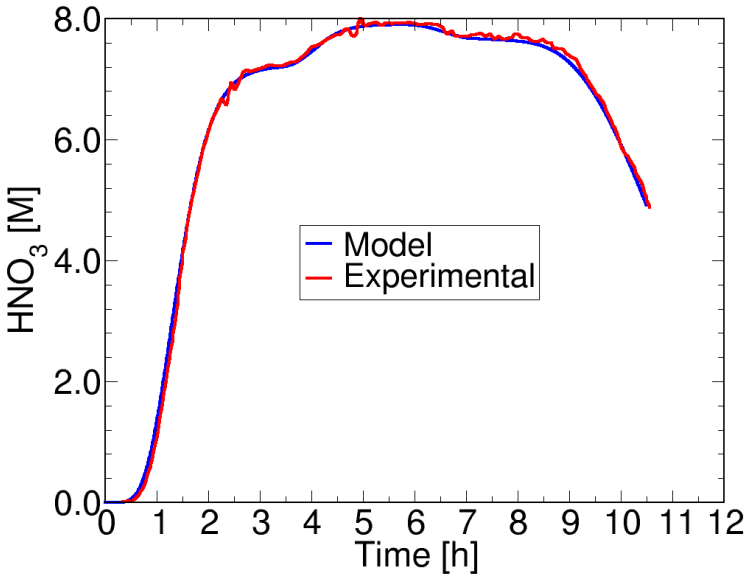

Fig. 8.3: *Nitric acid molarity variation in the feed compartment for model validation. Comparison of experimental and simulation data.*

evolution of the shape of a dissolving solid-liquid interface are necessary fidelity improvements for the plant level model.

Particle-size simulation of dissolution/leaching processes can be modeled and simulated on an off-line basis and the interfacial area obtained (de Almeida et al., 2012). Figure 9.1 presents recent simulation results for the dissolution of an inhomogeneous two-dimensional particle exposed to a flowing fluid from top to bottom. It is clear that an interfacial instability is prompted on an smoothly varying solid interface by the dissolving solution. Therefore the interface becomes rough which supports experimentally observed fuel particles dissolved in nitric acid.

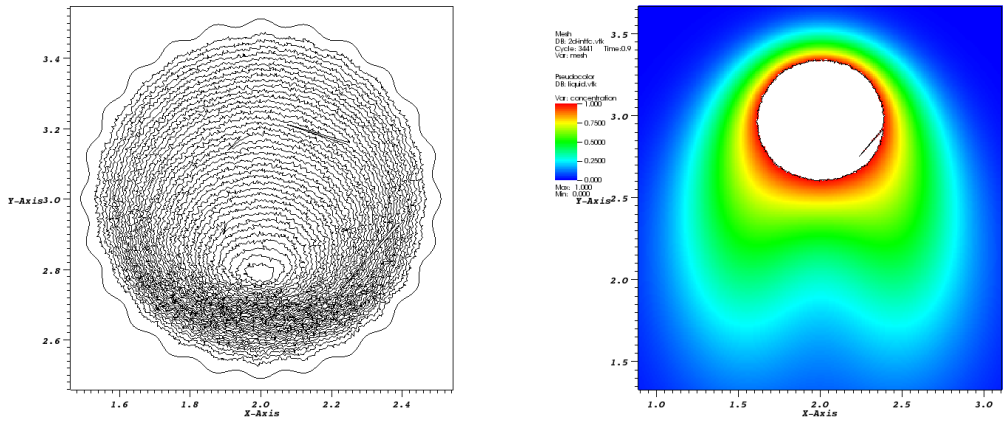

Fig. 9.1: *Dissolution of an inhomogeneous, two-dimensional particle in flowing fluid.* ***Left:*** *reduction of the perimeter of the initially smooth particle.* ***Right:*** *solute concentration around the dissolving particle showing a dissolution induced crack.*

Simulations of dissolution at the particle scale can provide improved substitutes for (4.8) which is currently a great source of error in the dissolver model. Future work on dissolution of solid particles should consider this approach for calibrating plant-level models. The preliminary subscale simulation presented here (fig. 9.1 is associated to an existing Nuclear Energy University Program project which is developing front tracking algorithms for fluid micromixing (Zhou et al., 2012).

10 Model transferability

The dissolver model presented in this report is based on a chemical themomechanical network theory advanced in an earlier report which has great potential for unifying the

mathematical modeling of a large class of processes. Therefore at the minimum, the model presented here is transferable to dissolution processes occurring in a different device. By virtue of the use of a network representation of contactor devices, a rational software development should be able to use various contactors without the need to modify the details of the chemical and/or mechanical processes; as explained in de Almeida (2011).

11 Comments and future work

This initial development of a mathematical model and its computational module implementation for a dissolver device applied generic concepts of modeling and simulation that naturally call for further improvements. Here, a prioritized list of future efforts for the internals of the model/module is suggested.

- Sensitivity analysis is a natural next step which can take advantage of the currently used DAE solver.
- Considerations of the gas/vapor phase should be added to the model; followed by sensitivity analysis.
- Non-isothermal conditions should be added by virtue of the energy balance equations.
- Mechanics of solids and fluid mixing should be added to the model through the power balance equations.
- Inclusion of other solids representative of sheared fuel rods could be added next.
- Development of a fluid capacity function via computational fluid mechanics, as mentioned earlier
- Calculations of partial molar volumes for representative liquid solutions could be done in parallel to the previous item.
- Kinetics of dissolution needs improvement either via a supporting experimental program or/and subscale modeling and simulation.

On the integration aspects of the model/module the following list of items should be considered.

- The current module written in MATLAB programing language supports the integration with Simulink for the SSPM code by saving the internal state at each SSPM function call for a pre-specified amount of time in the future. This time coupling requires testing and verification.

- The reverse communication where the dissolver module obtains time-dependent input data from the host code, SSPM, needs to be implemented through the module's interface.
- Additional work is needed on the Simulink side to allow for use of full MATLAB user-developed functions.

Acknowledgments

This work was sponsored by the U.S. Department of Energy through the Office of Nuclear Energy in the Nuclear Energy Advanced Modeling and Simulation project and the Separations working group in the Fuel Cycle Technologies program, under contract DE-AC05-00OR22725 with UT-Battelle, LLC.

A Appendix: Rotary dissolver CAD specification

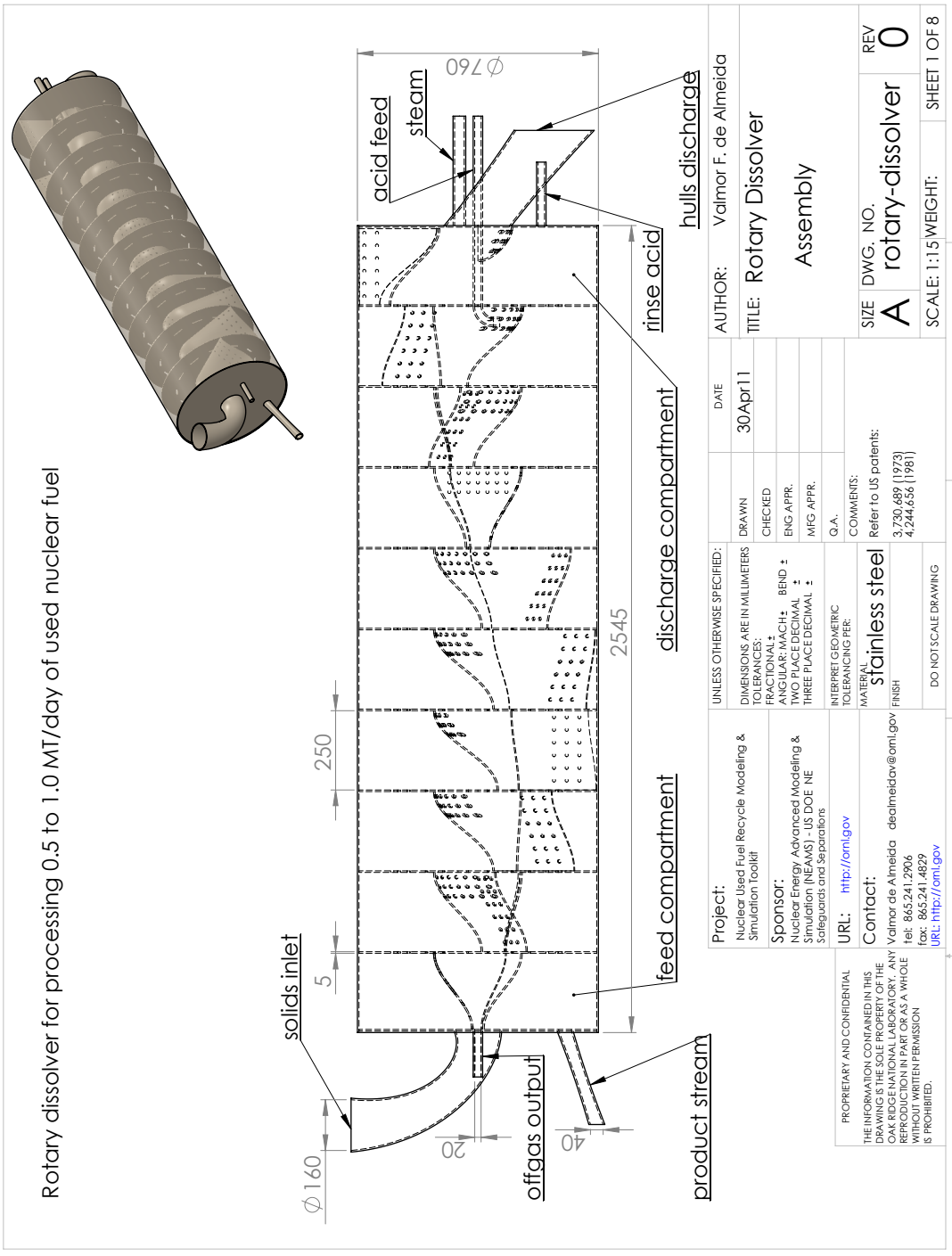

Fig. A.1: *Rotary dissolver CAD assembly drawing.*

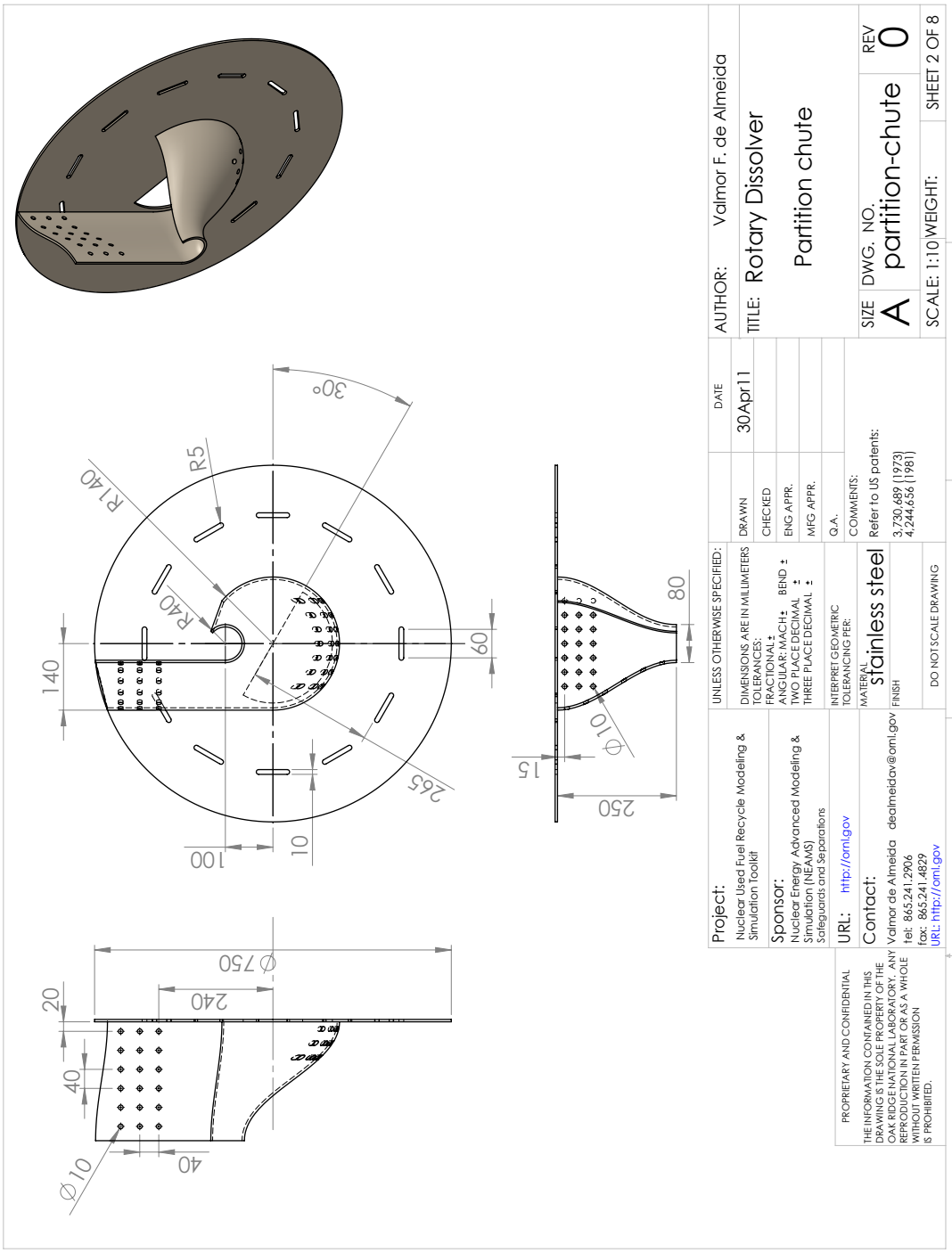

Fig. A.2: *Rotary dissolver CAD partition chute drawing.*

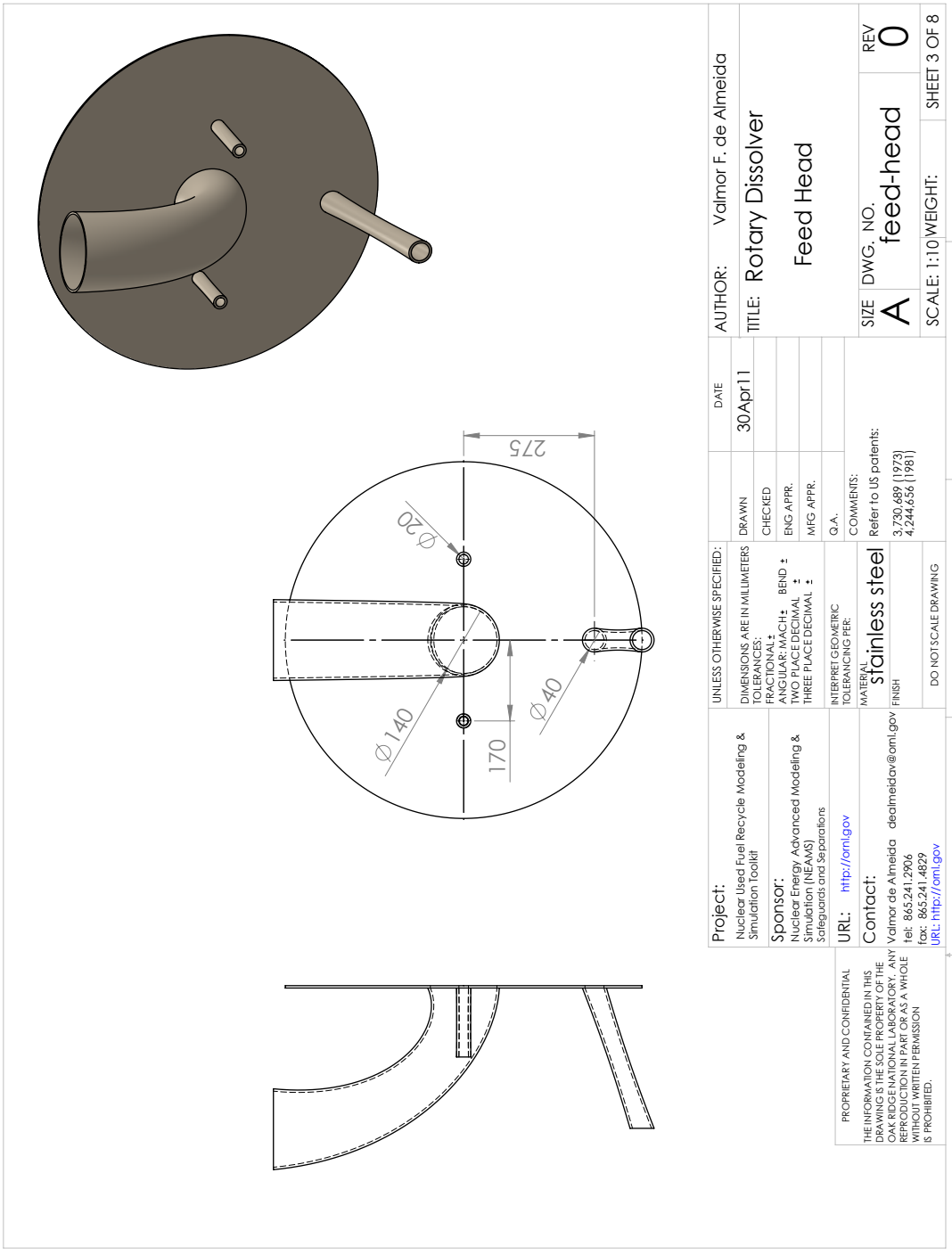

Fig. A.3: *Rotary dissolver CAD feed head drawing.*

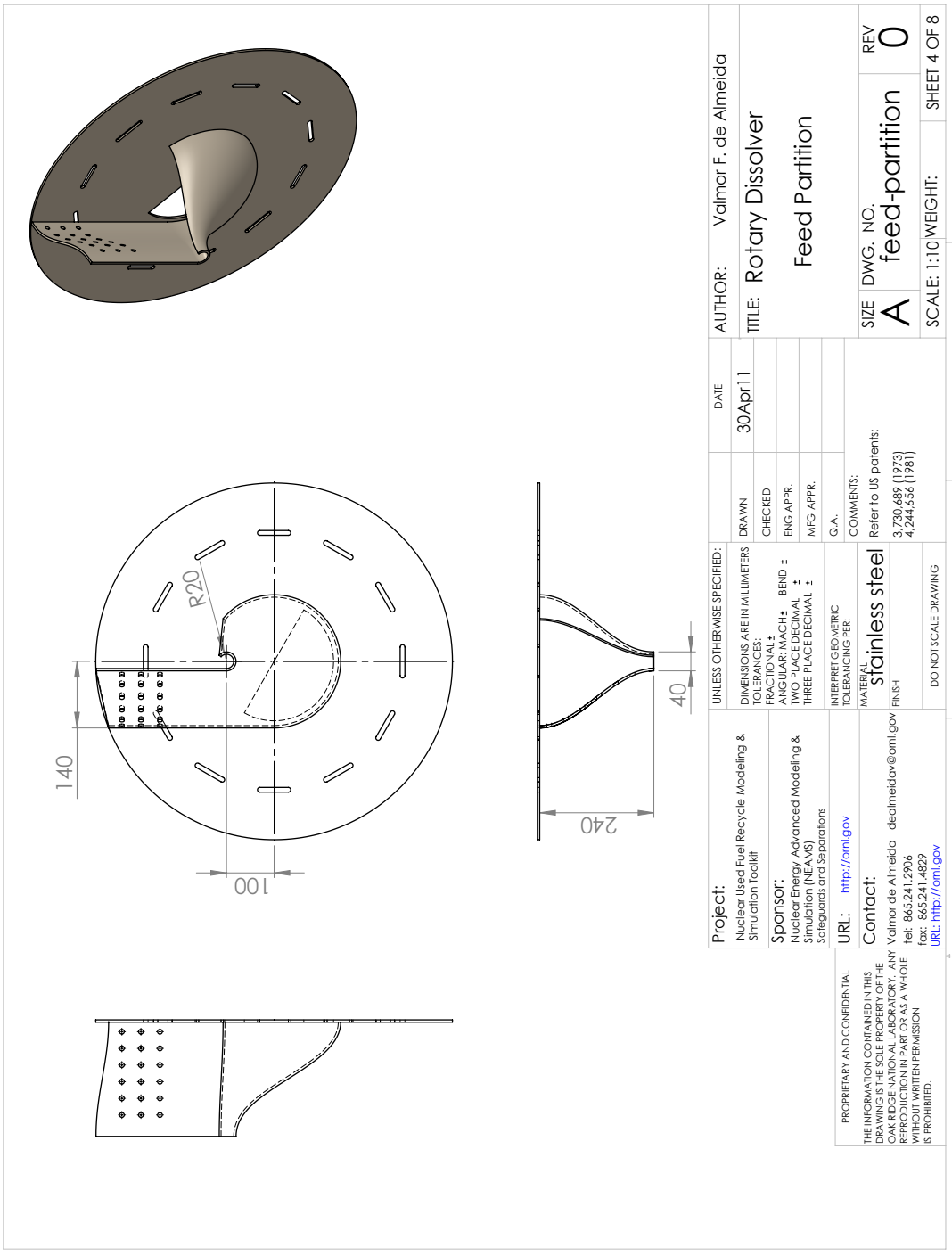

Fig. A.4: *Rotary dissolver CAD feed partition drawing.*

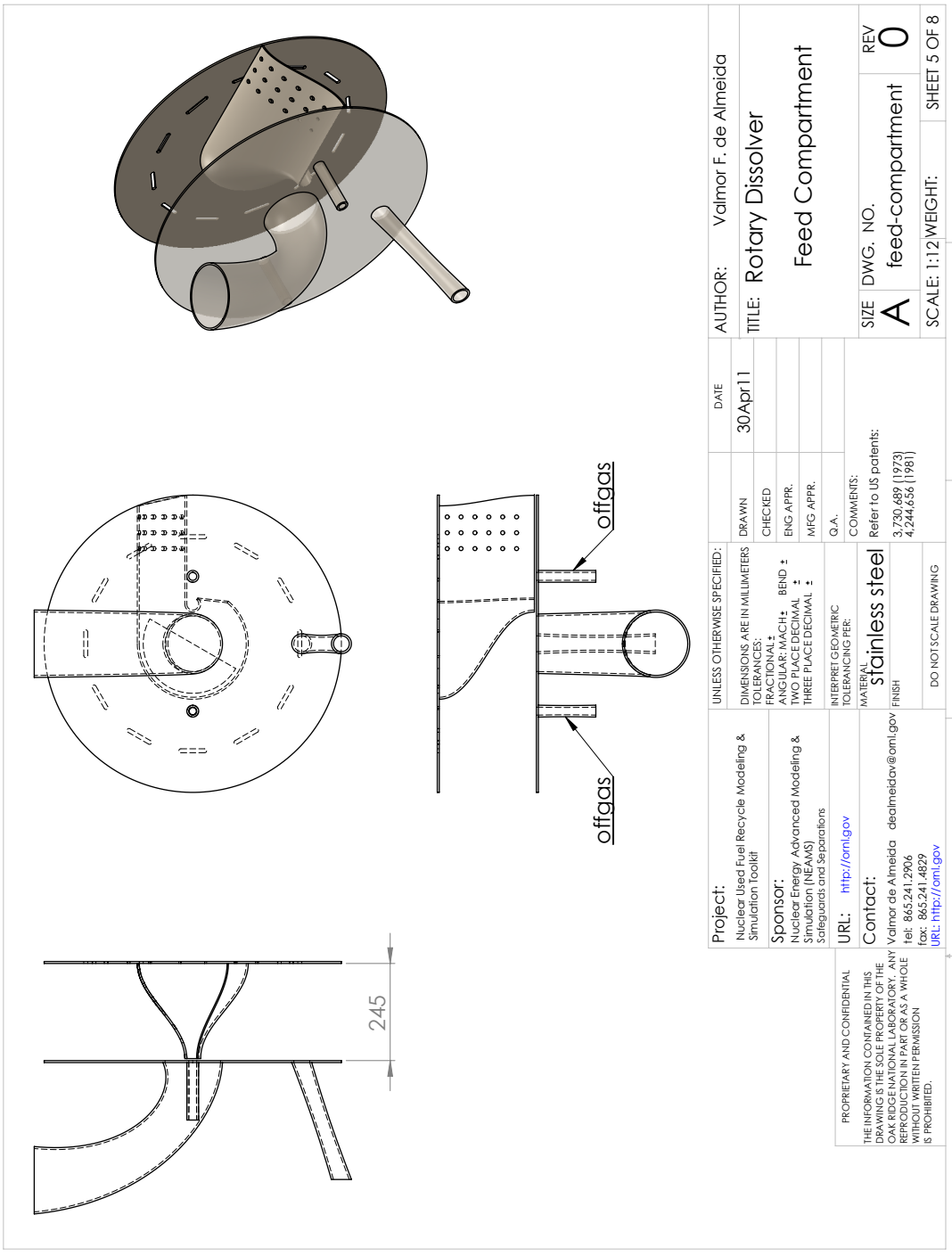

Fig. A.5: *Rotary dissolver CAD feed compartment drawing.*

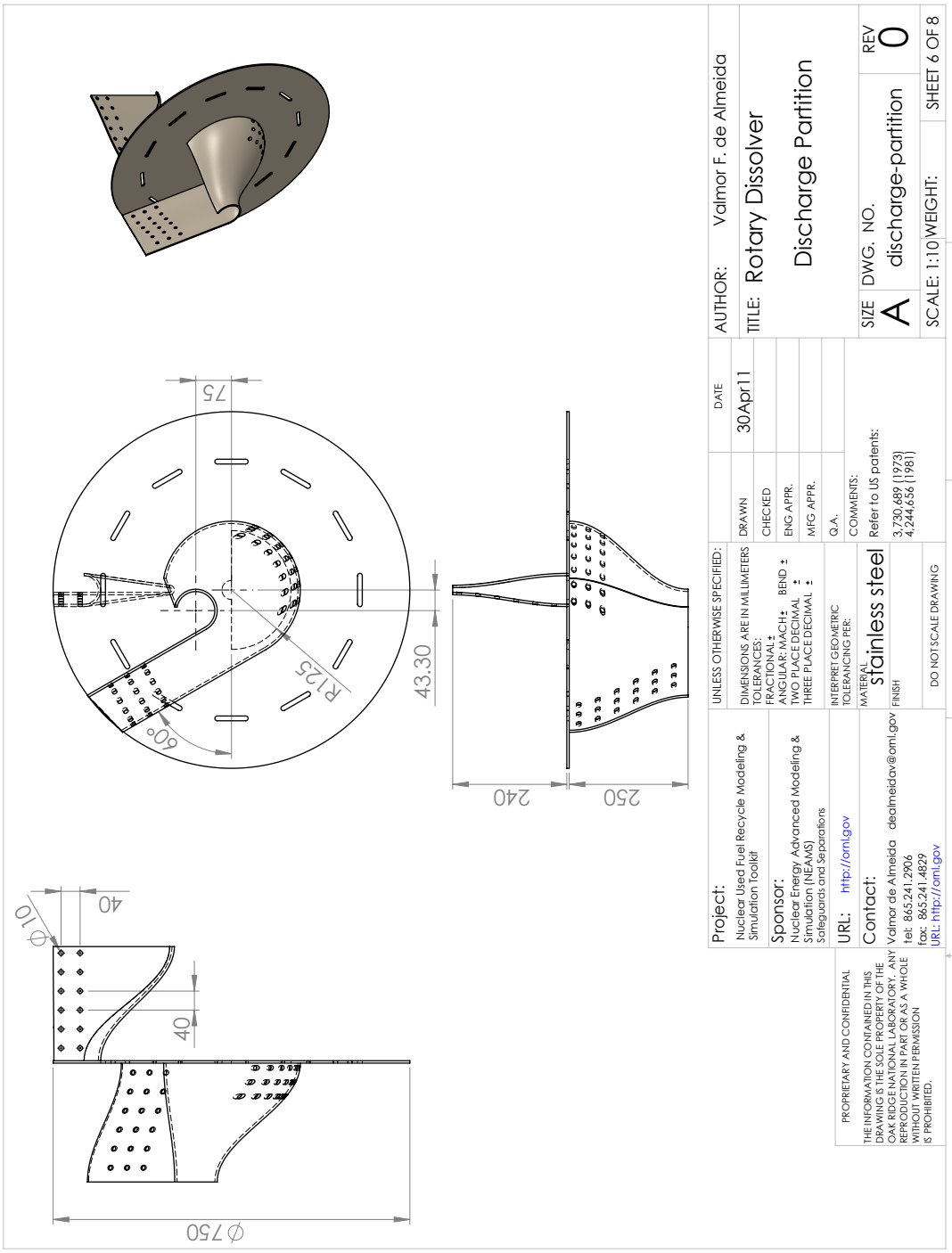

Fig. A.6: *Rotary dissolver CAD discharge partition drawing.*

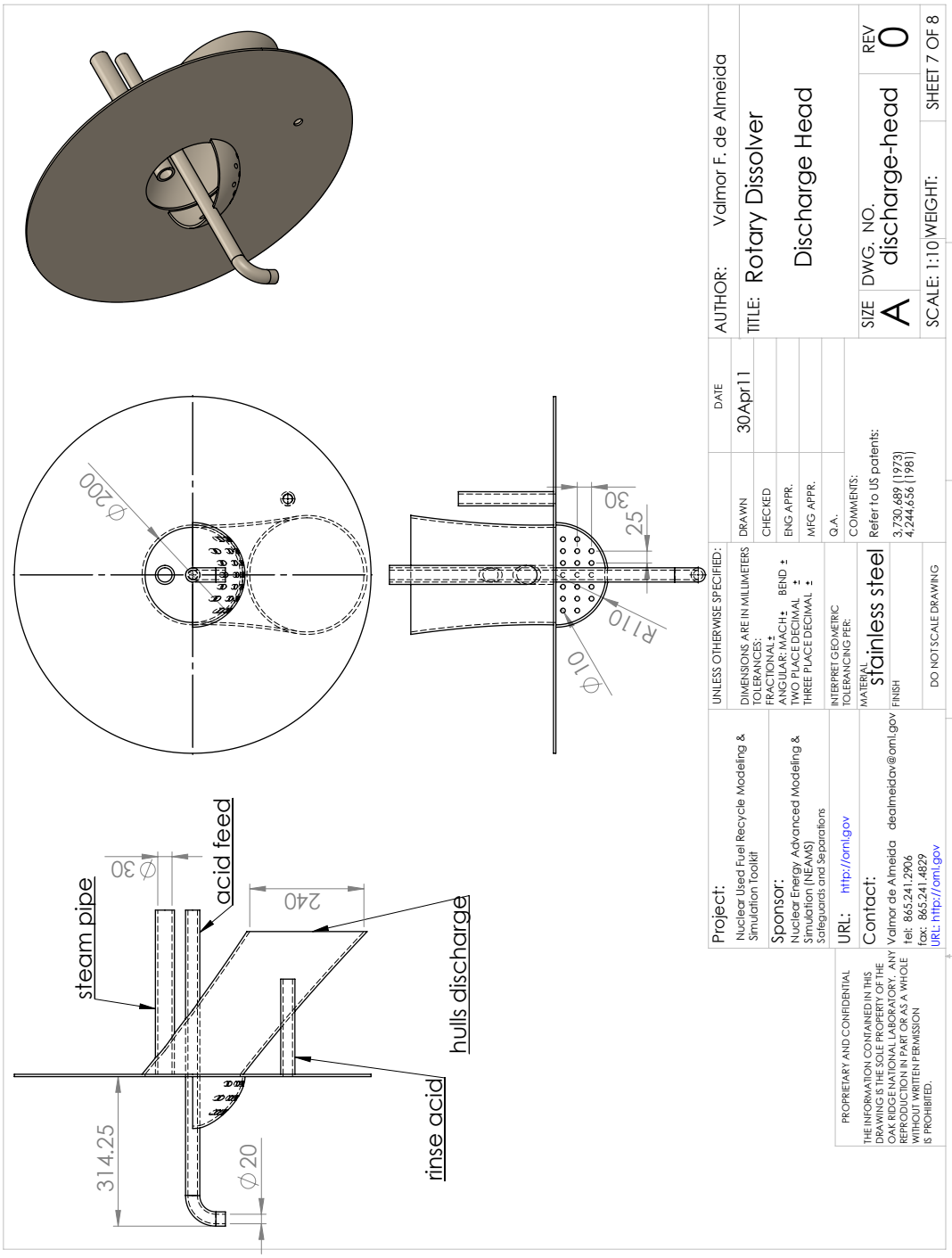

Fig. A.7: *Rotary dissolver CAD discharge head drawing.*

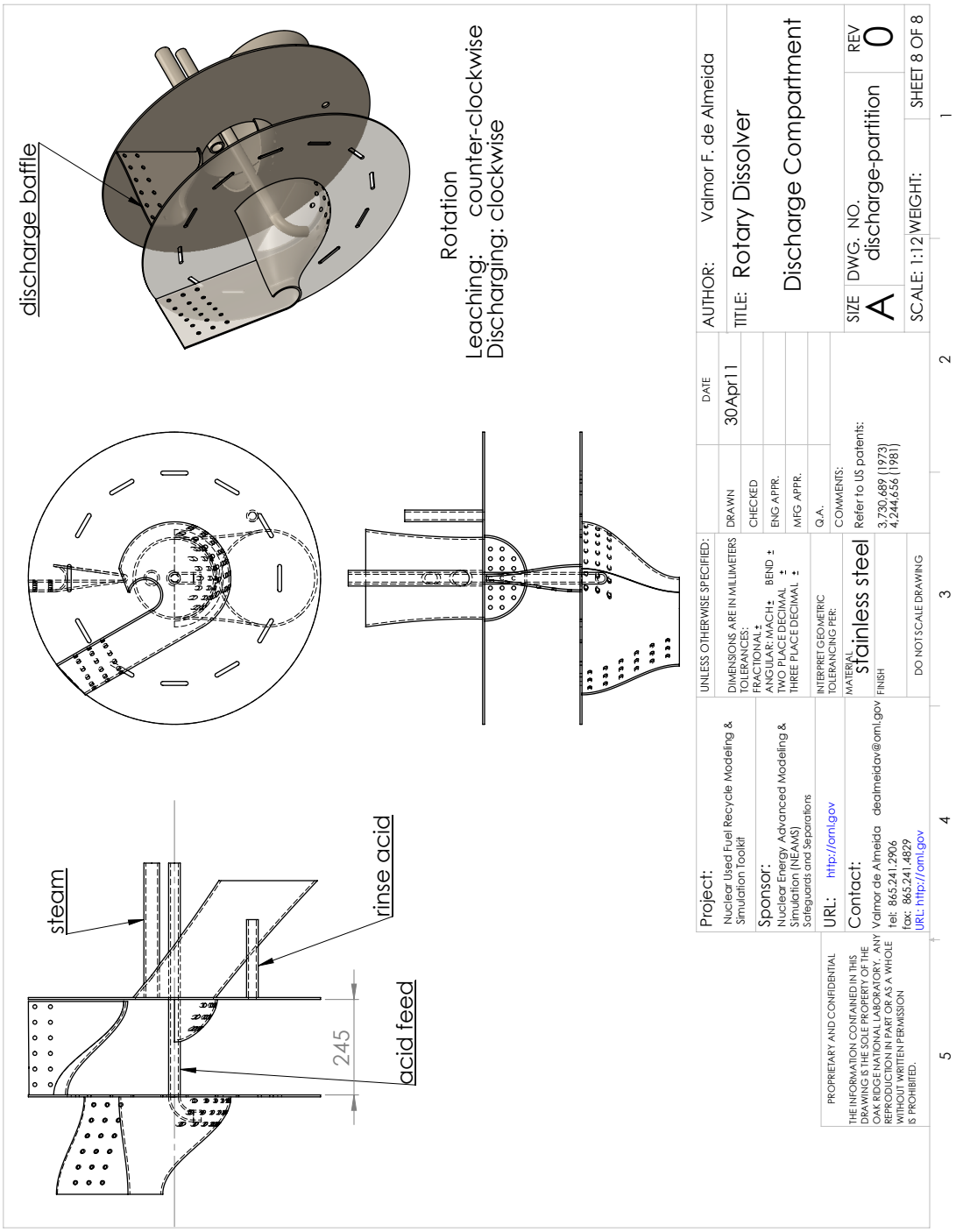

Fig. A.8: *Rotary dissolver CAD discharge compartment drawing.*

References

K. E. Brenan, S. L. Campbell, and L. R. Petzold. *Numerical Solution of Initial-Value Problems in Differential-Algebraic Equations*, volume 14 of *Classics in Applied Mathematics*. Society for Industrial and Applied Mathematics, Philadelphia, Pennsylvania, 1996. In 2011 the DASPK-3.1 source code could be downloaded from the URL: http://www.cs.ucsb.edu/ cse/Software/daspk31.tgz.

W. D. Burch, M. J. Feldman, W. S. Groenier, B. L. Vondra, and W. E. Unger. Advanced fuel recycle program progress report for period April 1st to June 30th. Technical Manuscript ORNL/TM-5993, Oak Ridge National Laboratory, Tennessee, TN 37831-6181, U.S.A., September 1977.

Benjamin B. Cipiti and Michael McDaniel. Reprocessing plant scale model integration. Sandial Report SAND2012-7779, Sandia National Laboratories, Albuquerque, New Mexico 87185, U.S.A., September 2011.

Benjamin B. Cipiti, Valmor F. de Almeida, Ian C. Gauld, Joseph F. Birdwell, and David W. DePaoli. Coupling a transient solvent extraction module with the separations and safeguards performance model. Sandial Report SAND2009-6307, Sandia National Laboratories, Albuquerque, New Mexico 87185, U.S.A., October 2009.

Valmor F. de Almeida. Progress on plant-level components for nuclear fuel recycling: Commonality. Letter Report ORNL/LTR-2011-176, Oak Ridge National Laboratory, Tennessee, TN 37831-6181, U.S.A., July 2011. Also available by request to `dealmeidav@ornl.gov`.

Valmor F. de Almeida, Yijing Hu, and Xiaolin Li. Dissolution of an inhmogeneous particle by front tracking simulation. Technical Manuscript Report ORNL/TM-2012-345, Oak Ridge National Laboratory, Tennessee, TN 37831-6181, U.S.A., December 2012. In preparation: available by request to `dealmeidav@ornl.gov`.

M. H. Ehinger. Process monitoring in international safeguards for reprocessing plants—a demonstration. Technical Manuscript ORNL/TM-10912, Oak Ridge National Laboratory, Tennessee, TN 37831-6181, U.S.A., January 1989.

Tetsuo Fukasawa, Yoshihiro Ozawa, and Fumio Kawamura. Comparative studies on the dissolution of ceramic UO_2 pellets in nitric acid by microwave and conventional heating. *Nucl. Technol.*, 94:108–13, 1991.

W. S. Groenier. Equipment for the dissolution of core material from sheared power reactor fuels. Technical Manuscript ORNL/TM-3194, Oak Ridge National Laboratory, Tennessee, TN 37831-6181, U.S.A., April 1971.

Shunji Homma, Jiro Koga, and Shiro Matsumoto. Dissolution rate equation of UO_2 pellet. *J. Nucl. Sci. Technol.*, 30:115–7, 1993. Short note.

Y. Ikeda, Y. Yasuike, K. Nishimura, S. Hasegawa, and Y. Takashima. Kinetic study on dissolution of UO_2 powders in nitric acid. *J. Nucl. Mater.*, 224:266–72, 1995.

Yasuhisa Ikeda, Yoshiyuki Yasuike, Kenji Nishimura, and Shimichi Hasegawa. Dissolution behavior of pulverized irradiated fuels in nitric acid solutions. *J. Nucl. Sci. Technol.*, 30:358–63, 1999.

H. F. Johnson. Analysis of UO_2 dissolution in nitric acid. Report ORNL-3297, Oak Ridge National Laboratory, Tennessee, TN 37831-6181, U.S.A., September 1962.

Patrick Knupp and Kambiz Salari. *Verification of Computer Codes in Computational Science and Engineering*. Discrete Mathematics and Its Applications. Chapman & Hall/CRC, Boca Raton, Florida, 2007.

Benjamin E Lewis. An unsteady-state material balance model for a continuous rotary dissolver. Technical Manuscript ORNL/TM-9019, Oak Ridge National Laboratory, Tennessee, TN 37831-6181, U.S.A., October 1984.

Benjamin E Lewis and F. E. Weber. A mathematical model for liquid flow transients in a rotary dissolver. Technical Manuscript ORNL/TM-7490, Oak Ridge National Laboratory, Tennessee, TN 37831-6181, U.S.A., October 1980.

E. L. Nicholson Jr. The PuO_2 dissolution problem for LWR plutonium recycle and LMFBR fuels: Fabrication and reprocessing problems and their resolution. Technical Manuscript ORNL/TM-5903, Oak Ridge National Laboratory, Tennessee, TN 37831-6181, U.S.A., July 1977.

Clyde H. Odom. Coninuous or semicontinous leacher for leaching soluble core material from sheared, spent nuclear fuel tubes. In *Proceedings of the* 20^{th} *Conference on remote systems techonology*, pages 101–112, 1972.

Clyde H. Odom and Maurice H. Kunselman. Apparatus for leaching core material from sheared segments of clad nuclear fuel pins, May 1973. United States Patent 3 730 689.

Armando L. Uriarte and Robert H. Rainey. Dissolution of high-density UO_2, PuO_2 and UO_2-PuO_2 pellets in inorganic acids. Report ORNL-3695, Oak Ridge National Laboratory, Tennessee, TN 37831-6181, U.S.A., July 1965.

O. O. Yarbro, D. R. Moser, T. W. Burgess, B. B. Spencer, P. Welesko, J. E. Dunn, W. W. Evans, and J. H. Shaffer. Integrated equipment test IET facility summary of operations for FY 1985. Technical Manuscript ORNL/TM-10084, Oak Ridge National Laboratory, Tennessee, TN 37831-6181, U.S.A., October 1986.

Orlan O. Yarbro. Apparatus for leaching core material from clad nuclear fuel pin segments, October 1980. United States Patent 4 230 675.

Yoshiyuki Yasuike, Yasuhisa Ikeda, and Yoichi Takashima. Kinetic study on dissolution of U_3O_8 powders in nitric acid. *J. Nucl. Sci. Technol.*, 32:102–4, 1995. Short note.

Yunfeng Zhao and Jing Chen. Studies on the dissolution kinetics of ceramic uranium dioxide particles in nitric acid by microwave heating. *J. Nucl. Mater.*, 373:53–8, 2008a.

Yunfeng Zhao and Jing Chen. Comparative studies on the dissolution of ceramic UO_2 pellets in nitric acid by microwave and conventional heating. *Radiochim. Acta*, 96: 467–71, 2008b.

Yijie Zhou, Navamita Ray, Hyunkyung Lim, Valmor F. de Almeida, James Glimm, Xiaolin Li, and Xiangmin Jiao. Development of a front tracking method for two-phase micromixing of incompressible viscous fluids with interfacial tension in solvent extraction. Report ORNL/TM-2012-28, Oak Ridge National Laboratory, Tennessee, TN 37831-6181, U.S.A., June 2012. Also available by request to `dealmeidav@ornl.gov`.